CrossMark

A SURVEY FOR Hα EMISSION FROM LATE L DWARFS AND T DWARFS[*]

J. Sebastian Pineda[1], Gregg Hallinan[1], J. Davy Kirkpatrick[2], Garret Cotter[3], Melodie M. Kao[1], and Kunal Mooley[3]

[1] California Institute of Technology, Department of Astronomy, 1200 E. California Avenue, Pasadena, CA 91125, USA; jspineda@astro.caltech.edu
[2] Infrared Processing and Analysis Center, MS 100-22, California Institute of Technology, Pasadena, CA 91125, USA
[3] University of Oxford, Department of Physics, Denys Wilkinson Building, Keble Road, Oxford, OX1 3RH, UK

ABSTRACT

Recently, studies of brown dwarfs have demonstrated that they possess strong magnetic fields and have the potential to produce radio and optical auroral emissions powered by magnetospheric currents. This emission provides the only window on magnetic fields in the coolest brown dwarfs and identifying additional benchmark objects is key to constraining dynamo theory in this regime. To this end, we conducted a new red optical (6300–9700 Å) survey with the Keck telescopes looking for Hα emission from a sample of late L dwarfs and T dwarfs. Our survey gathered optical spectra for 29 targets, 18 of which did not have previous optical spectra in the literature, greatly expanding the number of moderate-resolution ($R \sim 2000$) spectra available at these spectral types. Combining our sample with previous surveys, we confirm an Hα detection rate of $9.2^{+3.5}_{-2.1}\%$ for L and T dwarfs in the optical spectral range of L4–T8. This detection rate is consistent with the recently measured detection rate for auroral radio emission from Kao et al., suggesting that geometrical selection effects due to the beaming of the radio emission are small or absent. We also provide the first detection of Hα emission from 2MASS 0036 +1821, previously notable as the only electron cyclotron maser radio source without a confirmed detection of Hα emission. Finally, we also establish optical standards for spectral types T3 and T4, filling in the previous gap between T2 and T5.

Key words: brown dwarfs – stars: activity – stars: low-mass

1. INTRODUCTION

Twenty years ago, the discovery of the first brown dwarfs opened up the study of sub-stellar objects as interesting astrophysical targets spanning the gap between stars and planets (Nakajima et al. 1995; Oppenheimer et al. 1995). Since then, our understanding of brown dwarfs has developed considerably, including their atmospheric properties, evolution, and internal structure (e.g., Burrows et al. 2001; Kirkpatrick 2005; Marley & Robinson 2015 and references therein). Many of these developments are based on detailed spectroscopic analyses examining brown dwarf spectra at infrared (IR) wavelengths, where the photospheric flux is the brightest, and where the effects of absorption bands, such as CH_4, H_2O, and NH_3, are most prominent (e.g., Burgasser et al. 2002a, 2006a, 2006b, 2010; McLean et al. 2003; Knapp et al. 2004; Cushing et al. 2005, 2008, 2011; Stephens et al. 2009; Kirkpatrick et al. 2012; Mace et al. 2013). By comparison, the flux at red optical wavelengths (600–1000 nm) is much fainter because of the cool effective temperatures, especially for late L dwarfs, T dwarfs, and Y dwarfs ($T_{\rm eff} < 1500$ K). Consequently, there have been far fewer studies looking at cool brown dwarfs at these wavelengths.

One feature of particular interest in the optical spectrum is Hα emission at 6563 Å, which has often been used as an indicator of chromospheric emission in the spectra of M dwarfs and early L dwarfs (e.g., Reiners & Basri 2008; Schmidt et al. 2015). For early M dwarfs, the chromospheric nature of the Balmer emission is substantiated by accompanying evidence in X-ray and UV data, revealing high temperature

atmospheric regions consistent with a transition region between the photosphere and a corona (e.g., Linsky et al. 1982; Fleming et al. 1988; Walkowicz et al. 2008). For late M dwarfs, L dwarfs, and cooler objects, despite very few detections in the X-ray and UV, the presence of chromospheres has been inferred in the population based on detections of Hα emission and the analogy with the warmer stars. However, X-ray and optical observations of ultracool dwarfs (UCDs; spectral type ⩾M7) show a drop in their X-ray and Hα luminosities (Berger et al. 2010; Williams et al. 2014; Schmidt et al. 2015). The decline in these X-ray and Hα emissions, has been seen as indicative of a decline in the ability of UCDs to sustain much magnetic activity in their cool atmospheres with a transition taking place around the boundary between stars and brown dwarfs (Mohanty et al. 2002; Reiners & Basri 2008; Berger et al. 2010).

Despite the cool atmospheric temperatures, recent surveys have revealed that many brown dwarfs also show strong radio emission, indicating that they can sustain strong magnetic fields throughout the whole spectral sequence from L dwarfs to T dwarfs (Hallinan et al. 2008; Berger et al. 2010; Route & Wolszczan 2012; Williams et al. 2014; Kao et al. 2016). Early efforts to understand this radio emission invoked standard Solar-like magnetic processes (Berger 2006; Berger et al. 2009; Route & Wolszczan 2012). Building on those efforts, continued monitoring of the radio brown dwarfs and observations of the coolest UCDs have now shown that the pulsed radio emission is entirely consistent with being a consequence of the electron cyclotron maser instability (ECMI) as part of auroral currents in the magnetosphere (Hallinan et al. 2008, 2015; Lynch et al. 2015; Williams & Berger 2015; Kao et al. 2016). Furthermore, Hallinan et al. (2015) demonstrated that certain optical spectral features, Balmer series emission lines, and broadband variability, can be directly tied to the auroral process in some objects. The

connection is further corroborated by the association of radio aurorae with Hα emission, suggested by a high detection rate of radio brown dwarfs in the late L dwarf and T dwarf regime, when selecting the observational sample based on potential auroral activity indicators (Kao et al. 2016). This survey is in stark contrast to the very low detection rate of numerous previous surveys that looked for radio emission from brown dwarfs (Berger 2006; McLean et al. 2012; Antonova et al. 2013; Route & Wolszczan 2013).

Within the UCD regime, many objects may indeed exhibit chromospheric emissions, especially for the late M dwarfs and early L dwarfs, in which the atmospheres are warmest. However, many studies have now shown that auroral processes are also possible throughout the brown dwarf sequence. This leads to the questions: what governs brown dwarf magnetic activity and what drives potential auroral activity? Among late M dwarfs and early L dwarfs, disentangling the different processes requires dedicated monitoring of known benchmark objects like 2MASS 0746+2000 and LSR 1835+3259 (Berger et al. 2009; Hallinan et al. 2015). Another way to examine the question is to observe late L dwarfs and T dwarfs, objects in which the local stochastic heating of the upper atmosphere that generates chromospheric emission, as seen on the Sun, is difficult to generate. A study of the activity in these objects allows us to understand the prevalence of magnetic processes, assess the viability of the auroral mechanism and find new potential benchmark targets for dedicated monitoring. If the Hα emission in these objects is associated with the same processes that produce auroral radio emission, surveys in the optical provide an additional means to look for brown dwarfs potentially harboring auroral activity. The advantage of surveying for magnetic activity in the optical, over the radio, is that at radio wavelengths the emission may be highly beamed, as in the auroral case, and thus a detection can be highly dependent on the viewing geometry of the system, but is less dependent on geometry at optical wavelengths (Treumann 2006). These factors motivate the search for Hα emission, potentially of an auroral nature, in the optical spectrum. We note that optical variability due to weather phenomena is also a compelling reason to observe and monitor the spectra of objects in this spectral range (Heinze et al. 2015).

Our focus is on late L dwarfs and T dwarfs which have received less followup at optical wavelengths than the warmer brown dwarfs but are much brighter in the optical than the cooler Y dwarfs. Much of these initial efforts took place ~10 years ago, prominently by Kirkpatrick et al. (1999), Burgasser et al. (2003), and Cruz et al. (2007), hereafter K99, B03, and C07, respectively. The early studies were not able to get detailed optical spectra for all of the brown dwarfs that emerged from early wide-field IR sky surveys like the Two Micron All Sky Survey (2MASS; Skrutskie et al. 2006). Moreover, since then, numerous all sky surveys, including the Sloan Digital Sky Survey (SDSS; York et al. 2000), the DEep Near-IR Survey of the Southern Sky (DENIS; Epchtein et al. 1997), the *Wide-field IR Survey Explorer* (*WISE*; Wright et al. 2010), the Panoramic Survey Telescope and Rapid Response System (Kaiser et al. 2002), the United Kingdom IR Telescope Deep Sky Survey (Lawrence et al. 2007), and the Canada–France–Hawaii Telescope Legacy Survey (Delorme et al. 2008), have greatly expanded the number of known late L dwarfs and T dwarfs, many of them bright enough to observe with large ground-based telescopes. The growing number of

late L dwarfs and T dwarfs, thus allows for a comprehensive assessment of the prevalence of Hα activity for objects of this effective temperature range.

Due to the small number of T-dwarf studies at optical wavelengths, our current observational understanding of their spectra remains defined by the early works, like B03, and the few handful of targets they observed. These early spectra set the optical spectral sequence in this regime and provide the observational archetypes for T dwarf optical spectral features (Kirkpatrick 2005). The prominent features include the pressure-broadened wings of the K I resonant doublet at 7665/7699 Å, other alkali lines from Cs I and Rb I, as well as molecular band-heads of CrH and H$_2$O (B03; Kirkpatrick 2005). These features are physically interesting because they are sensitive to temperature, gravity, metallicity, and the rainout of cloud condensates (Burrows et al. 2002). An expanded collection of optical spectra will thus allow us to examine these features in greater detail.

In this article, we present the results of a new survey of late L dwarfs and T dwarfs at red optical wavelengths looking for Hα emission. In Section 2, we discuss our observations and the target selection for our data sample. In Section 3, we present the collection of optical spectra, including literature data and examine the variety of optical spectral features. In Section 4, we focus in particular on the Hα emission and the prevalence of potential auroral activity. In Section 5, we discuss our findings for a series of particularly interesting objects in our data sample. Finally, in Section 6, we summarize and discuss our results.

2. DATA

2.1. Sample

We selected our target sample by examining the collection of known brown dwarfs in the literature and culling targets that already had observations at red optical wavelengths. We used the compendium of brown dwarfs at DwarfArchives.org as a resource in this endeavor, including new updates to the archive (C. Gelino, private communication) and also cross checked the Ultracool RIZzo Spectral Library.[4] We gave priority to the brightest and closest targets, using the Database of Ultracool Parallaxes[5] to verify the distances (Dupuy & Liu 2012). We further combined our new observations of these targets with literature T dwarf spectra (discussed in Section 2.2). All together this resulted in the largest compilation of late L dwarf and T dwarf red optical spectra yet assembled.

2.2. Observations

We observed our target brown dwarfs at the W. M. Keck Observatory using either the Low Resolution Imaging Spectrometer (LRIS) on Keck I or the DEep Imaging Multi-object Spectrograph (DEIMOS) on Keck II during the course of several observing nights, mostly in 2014 (Oke et al. 1995; Faber et al. 2003). The observations were designed predominately for the purposes of searching for Hα emission in objects without previous observational limits on the emission strength. However, in our survey, we also looked at some objects with previous limits, testing for variability, as well as at targets that may have only had marginal detections, which we sought to

---

Table 1
Observing Log

Object	SpT NIR/Opt[a]	UT Date	Filter	Instrument	t_{exp} (s)	Air Mass	References[b]
SDSS J000013.54+255418.6	T4.5/ T5	2014 Dec 22	OG550	DEIMOS	2400	1.18–1.25	(15), (5)
2MASS J00361617+1821104[c]	L3.5/L3.5	2012 Jul 19	Clear	LRIS	5400	1.00–1.10	(16)/(13), (17)
SIMP J013656.5+093347.3	T2.5/ T2	2014 Dec 22	OG550	DEIMOS	3600	1.01–1.10	(1)
		2014 Aug 27	OG550	LRIS	2400	1.02–1.03	⋯
2MASS J02431371−2453298	T6/ T5.5	2014 Dec 22	OG550	DEIMOS	2400	1.47–1.52	(4), (5)
SDSS J042348.57−041403.5	T0/ L7.5	2014 Dec 22	OG550	DEIMOS	1800	1.10	(11), (5)
2MASS J05591914−1404488	T4.5/ T5	2014 Dec 22	OG550	DEIMOS	2400	1.21–1.23	(3), (5)
WISEP J065609.60+420531.0	T3/ T2	2014 Dec 22	OG550	DEIMOS	2400	1.08	(14)
2MASS J07003664+3157266[d]	—/ L3.5	2014 Feb 03	GG400	DEIMOS	1200	1.24	(20)
2MASS J07271824+1710012	T7/ T8	2014 Feb 03	GG400	DEIMOS	1800	1.27	(4), (5)
SDSS J075840.33+324723.4	T2/ T3	2014 May 05	GG495	DEIMOS	2400	1.21–1.28	(15), (5)
WISE J081958.05−033528.5	T4/ T4	2014 May 05	GG495	DEIMOS	2400	1.09–1.10	(14)
2MASSI J0835425−081923	—/ L5	2014 Feb 03	GG400	DEIMOS	1200	1.35	(7)
SDSSp J092615.38+584720.9	T4.5/ T5	2014 Dec 22	OG550	DEIMOS	2400	1.35–1.38	(11), (5)
2MASS J09393548−2448279	T8/ T8	2014 Feb 03	GG400	DEIMOS	2000	1.57	(19), (5)
2MASS J10430758+2225236	—/ L8	2014 Dec 22	OG550	DEIMOS	2400	1.03–1.06	(8)
SDSS J105213.51+442255.7	T0.5/ L7.5	2014 May 05	GG495	DEIMOS	3600	1.10–1.12	(6)
2MASS J11145133−2618235	T7.5/ T8	2014 Feb 03	GG400	DEIMOS	2000	1.47	(19), (5)
2MASS J12314753+0847331	T5.5/ T6	2014 Dec 22	OG550	DEIMOS	2400	1.18–1.25	(15), (5)
SDSS J141624.08+134826.7	L6/ L6	2014 May 05	GG495	DEIMOS	1800	1.05	(2)
WISEP J150649.97+702736.0	T6/ T6	2014 May 05	GG495	DEIMOS	2000	1.42	(14)
2MASSW J1507476−162738	L5.5/ L5	2014 May 05	GG495	DEIMOS	900	1.25	(16)/(13), (15)
SDSSp J162414.37+002915.6	T6/ T6	2014 May 05	GG495	DEIMOS	1800	1.07	(18), (5)
PSO J247.3273+03.5932[e]	T2/ T3	2014 May 05	GG495	DEIMOS	1800	1.12	(9)
WISEP J164715.59+563208.2	L9p/ L7	2014 May 05	GG495	DEIMOS	2000	1.42	(14)
2MASS J17502484−0016151	L5.5/ L5	2014 May 05	GG495	DEIMOS	900	1.07	(12)
2MASS J17503293+1759042	T3.5/ T4	2014 May 05	GG495	DEIMOS	1200	1.07	(11), (5)
2MASS J17545447+1649196	T5.5/ T5.5	2014 May 05	GG495	DEIMOS	1800	1.11	(16)
2MASS J21392676+0220226	T1.5/ T2	2014 Aug 27	OG550	LRIS	2400	1.07–1.09	(10)
2MASS J22541892+3123498	T4/ T5	2014 Dec 22	OG550	DEIMOS	2400	1.12–1.17	(4), (5)

Notes.
[a] Optical spectral types are from this paper. For NIR spectral types see references.
[b] The first entry is the discovery reference and second the NIR spectral type reference unless otherwise noted.
[c] 2MASS J00361617+1821104—optical spectral type from Kirkpatrick et al. (2000); observations were taken with the LRIS Dichroic, D560.
[d] 2MASS J07003664+3157266—optical spectral type from Thorstensen & Kirkpatrick (2003).
[e] R.A. = 16 29 18.409, decl. = +03 35 37.10.

References. (1) Artigau et al. (2006), (2) Bowler et al. (2010), (3) Burgasser et al. (2000b), (4) Burgasser et al. (2002a), (5) Burgasser et al. (2006b), (6) Chiu et al. (2006), (7) Cruz et al. (2003), (8) C07, (9) Deacon et al. (2011), (10) Faherty et al. (2012), (11) Geballe et al. (2002), (12) Kendall et al. (2007), (13) Kirkpatrick et al. (2000), (14) Kirkpatrick et al. (2011), (15) Knapp et al. (2004), (16) Reid et al. (2000), (17) Reid et al. (2001), (18) Strauss et al. (1999), (19) Tinney et al. (2005), (20) Thorstensen & Kirkpatrick (2003).

confirm. The full observing log for the 29 objects is presented in Table 1. We also display the spectra of the 18 objects without previous optical spectra in Figures 1 and 2.

2.2.1. DEIMOS

The majority of our survey was conducted with Keck/DEIMOS, a multi-slit imaging spectrograph designed for acquiring optical wavelength spectra of faint objects. DEIMOS operates at the Nasmyth focus and includes a flexure compensation system for increased stability. The multi-slit capability utilizes pre-milled masks, however, we used the instrument in longslit mode with the standard longslit masks, placing the targets in the 1″ (8.4 pixels) wide slit. This mode is regularly used for spectroscopic followup for the Palomar Transient Factory (PTF; Law et al. 2009). The detector uses a large format 8k × 8k CCD mosaic, consequently the blue and red ends of a single spectroscopic exposure fall on different CCD chips with a small gap between them.

For our observations, we used the 600 line mm^{-1} grating blazed at 7000 Å yielding a wavelength coverage from 5000–9700 Å and a resolution of 3.5 Å ($R \sim 2000$) with a dispersion of 0.62 Å pixel^{-1}. The blue extent of the spectra were also limited by the use of order blocking filters to limit the effects of second order light (see Table 1). In comparison to the earlier observations in K99, B03, and C07, our observations are at a slightly higher resolution.

Data reduction for these observations was initiated with a modified version of the DEEP2 pipeline utilized by PTF (Cooper et al. 2012; Newman et al. 2013). The pipeline uses the overscan region to bias subtract the raw frames, median combines the dome flats to flat field the raw data, determines the wavelength solution from NeArKrXe arc lamps, and returns the two-dimensional spectrum of each slit for both the red and blue CCD chips with cosmic-ray rejection routines applied.[6]

---

[6] The longslit masks that we used have short breaks along the length of the slit to prevent the slitmask from buckling.
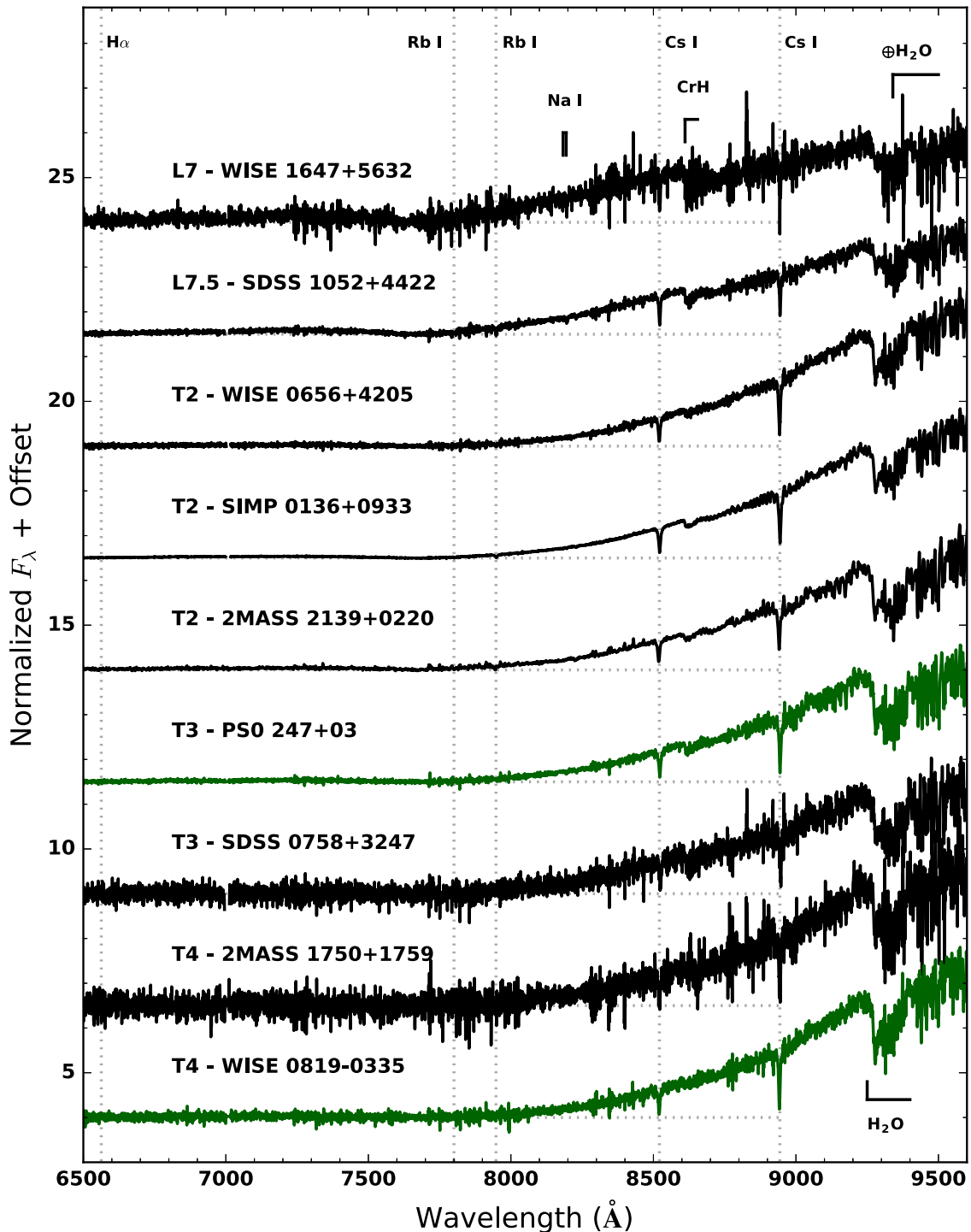
Figure 1. Sequence of spectra for objects in our sample without optical spectra in the literature, arranged according to the optical spectral type. The spectra are normalized at 8750 Å with some of the main spectral features noted—see also Figure 3. We also note the spectra of objects PSO 247+03 and WISE 0819–0335 as candidates for the optical T3 and T4 spectral standards (shown in green). Note that there is a slight break in the DEIMOS spectra at 7010 Å due to a gap in the DEIMOS detector. All the spectra plotted here were taken with DEIMOS, except for the spectrum of 2MASS J2139+02, which was taken with LRIS.

The rest of the data reduction was handled by custom routines in Python with PyRAF to rectify the frames, extract the spectra and flux calibrate.[7]

Since the UCDs have very red spectra, up to a couple orders of magnitude flux difference between 7000 and 9000 Å, for most targets the spectral flux is barely seen toward the blue end of the detector ($\lambda \lesssim 7000$ Å). Thus, the extractions for each CCD chip were done independently and we therefore used the location of the centroid of the target trace on the red chip in the rectified frames as the central location for the blue chip. We verified that this produced accurate results based on the
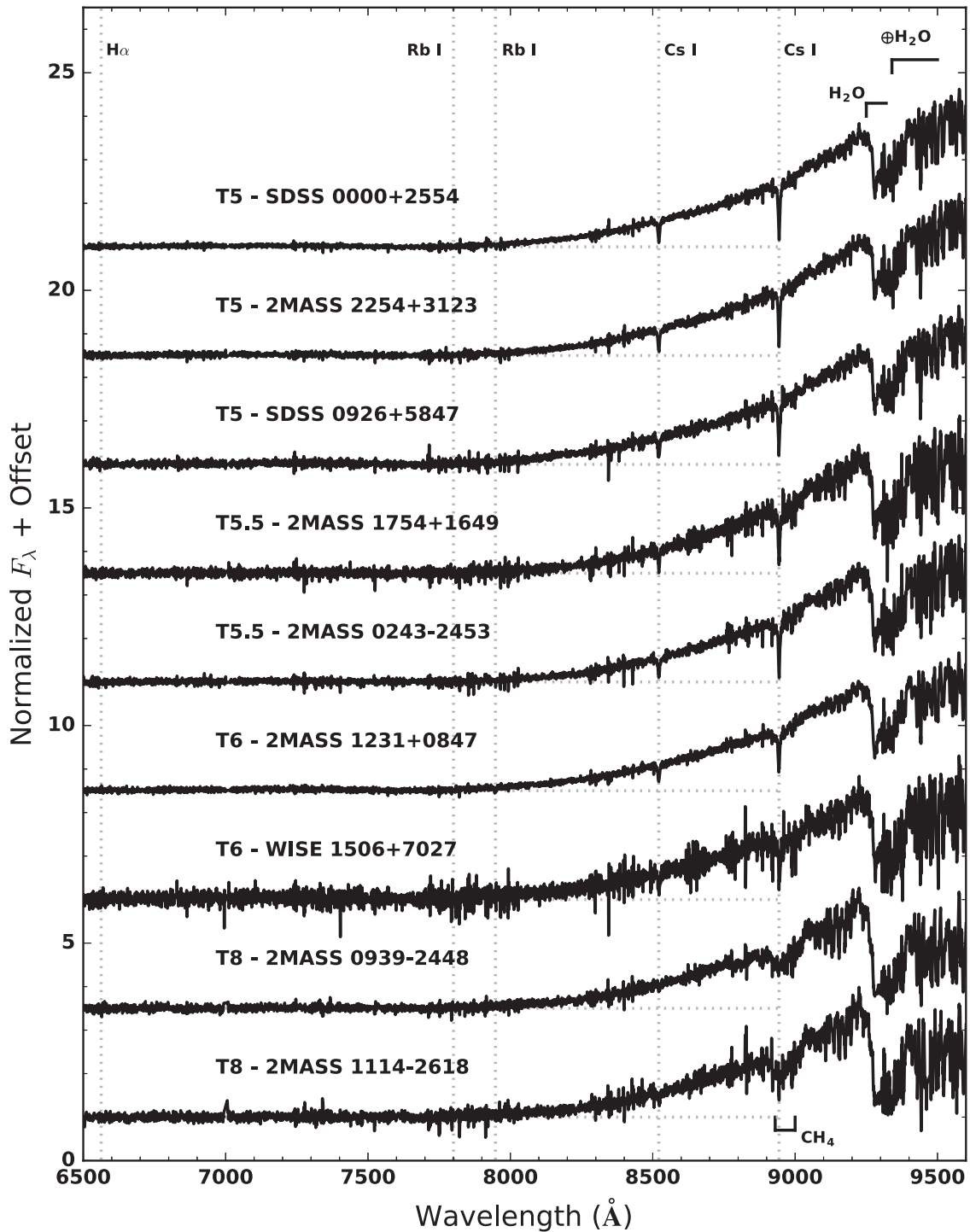
Figure 2. Continued from Figure 1.

calibration targets and the brighter L dwarfs with plenty of flux for $\lambda \lesssim 7000$ Å.

Our observations took place on 2014 February 3, May 5, and December 22 (UT). At the beginning of the observing night for February 3 there was fog at the summit, however, the dome opened up half way through the night with typical seeing conditions of 1″.2 . Conditions on May 5 were more favorable, with low humidity and 0″.8 seeing. December 22 was also a good observing night with good conditions throughout and 0″.7 seeing. Typical exposure times varied between 900 s for the L

dwarfs and up to 1800 s for the fainter T dwarfs with multiple exposures for some of the targets. We also observed a standard star from Hamuy et al. (1994) or Massey & Gronwall (1990) each night for the purposes of flux calibrating the spectra. These calibrators were Hiltner 600, HZ44, and Feige 110, respectively, for the three nights. We note that the specific order blocking filter varied for each of the three nights, GG400, GG495, and OG550, respectively.

Although, this did not effect the primary goal of surveying for $H\alpha$ emission, unlike the other filters, the use of the GG400

filter (observations on February 3) limited the ability to flux calibrate the red end of the spectrum due to contamination from second-order short wavelength light in the standard star observations. Consequently, we had to make adjustments in order to get flux calibrated spectra for that observing night. We took advantage of the fact that a couple of L dwarf targets we observed that evening, were part of the Ultracool RIZzo spectral library. To get a sensitivity curve for the red chip on that night, we divided the raw extracted spectrum by the literature spectra of the same targets, 2MASSI J0835425–081923 and 2MASS J07003664+3157266AB, took the median of the respective curves, and fit a low-order polynomial. We subsequently scaled the resulting curve to match the sensitivity function from the blue chip where there was no effect from the second order light. The resulting sensitivity curve agreed reasonably well with similar curves from the other observing nights and the reduced spectra from the night of February 3 proved to match the expected optical standards rather well (see Section 3.1).

The red end of the DEIMOS spectrum cuts off at ~9700 Å in the middle of a broad telluric H_2O absorption band. This presented an added difficulty in determining the flux calibration for a given night because the telluric band could not be interpolated over when determining the sensitivity function from the spectrophotometric standards. Consequently, the sensitivity function for $\lambda > 9300$ Å is based solely on the polynomial fit at shorter wavelengths. The effect this has on the spectral shape is only significant beyond ~9400 Å where the spectrum is also significantly effected by telluric absorption. Additionally, we did not correct for telluric absorption in any of the DEIMOS spectra. Thus, the effects of the telluric absorption are most prominent in the same region where the flux calibration is most unreliable. This has no impact on the bulk of our analysis as we focus on short wavelength regions, however it does have a small effect on the measurement of the H_2O feature at 9250 Å (see Section 3.2.2; B03).

2.2.2. LRIS

We observed the spectrum of 2MASS J00361617+1821104 (2MASS 0036+1821) on 2012, July 19. These observations used the 1200 line mm^{-1} grating blazed at 6400 Å through a 0″7 slit, yielding a wavelength coverage of 5600–7200 Å and a resolution of ~1.7 Å ($R \sim 3700$). The detector was readout with 2 × 2 binning, yielding a dispersion of 0.81 Å pixel^{-1}. The target was observed for 5400 s split into six 900 s exposures. The observations also used the LRIS dichroic D560 with a clear filter through the red arm of the instrument. We also took data with the blue side of LRIS, however, we do not present that data in this paper. These data were reduced with the `longslit` routines in IRAF.[8] The individual exposures were bias subtracted; corrected for pixel-to-pixel gain variation and slit illumination via dome flats; transformed onto a rectilinear wavelength-sky position grid via internal arc lamps; and finally sky-subtracted by interpolating a polynomial along each row in the sky direction, excluding the target from the fit by sigma-clipping.

We acquired LRIS spectra of SIMP J013656.5+093347.3 (SIMP 0136+0933) and 2MASS J21392676+0220226

(2MASS 2139+0220) on 2014 August 27. Although LRIS is designed to use a beamsplitter to allow independent and simultaneous observations in a red channel and a blue channel, these observations made use of only the red channel. Since the work of K99 and B03, which used LRIS to obtain optical spectra of late L dwarfs and T dwarfs, the red channel detector has been upgraded, improving the sensitivty (Rockosi et al. 2010).

Our observations on 2014 August 27 used the 400 line mm^{-1} grating blazed at 8500 Å through a 0″7 slit, yielding a wavelength coverage of 6300–10100 Å, a resolution of ~5 Å ($R \sim 1700$), and a dispersion of 1.33 Å pixel^{-1}. The data were taken through a companion program, and accidentally left out the order blocking filter, which meant the flux calibration was not viable from that night's observing (the dichroic was also set to clear). As we did with the February 3 DEIMOS observations (see Section 2.2.1), we used the flux calibrated DEIMOS observations of SIMP 0136+0933 from 2014 December 22, to calibrate for the rough shape of the LRIS sensitivity function. This did not effect the blue end of the spectrum, nor our ability to measure the Hα emission, however it created an effective upper limit to the LRIS wavelength coverage of 9700 Å. We reduced the data using standard routines in `PyRAF`. Since the spectral trace becomes very faint in the red, we used the trace for calibration white dwarfs taken before and after the science observations to define the extraction trace for our target brown dwarfs.

In our sample we also include the archival data of the 7 T dwarfs with red optical spectra from the *WISE* followup of Kirkpatrick et al. (2011), in order to bolster the sample size of T dwarf optical spectra and provide comparisons of the optical features across the full optical sequence to the latest T dwarf spectral types. These objects are, the T5, WISE 1841+7000, the T7s, WISE 1019+6529, and WISE 2340–0745, the T8s, WISE 1617+1807, WISE 1457+5815, and WISE 1653+4444, and the T9, WISE 1741+2553. These observations also used Keck/LRIS with similar settings but a wider 1″ slit. The reductions and calibrations of those data are described in K99 and Kirkpatrick et al. (2006). These objects were incorporated into the analysis of the optical spectral features (Section 3.2) but not for Hα emission (Section 4).

We also used the archival spectra of SDSSp J083717.22–000018.3, SDSSp J102109.6–030419, and 2MASS J12095613–1004008 to get additional measurements of T dwarf Hα emission (Kirkpatrick et al. 2008). These objects already had measurements of the important optical spectral features (see Section 3.2) but required flux estimates of their Hα emission instead of just equivalent widths (see Section 4).

3. OPTICAL SPECTRA

3.1. Spectral Sequence

To determine the optical spectral types for each object with new optical spectra, we compared the spectra visually with the set of optical spectral standards from L5 to T8. The optical standards are DENIS 1228–1547 for L5 (K99), 2MASS 0850 +1057 for L6 (K99), DENIS 0205–1159 for L7 (K99), 2MASS 1632+1904 for L8 (K99), SDSS 0837–0000 for T0 (Kirkpatrick et al. 2008), SDSS 1254–0122 for T2 (B03), 2MASS 0559–1404 for T5 (B03), SDSS 1624+0029 for T6 (B03), 2MASS 0415–0935 for T8 (B03), and WISE 1741
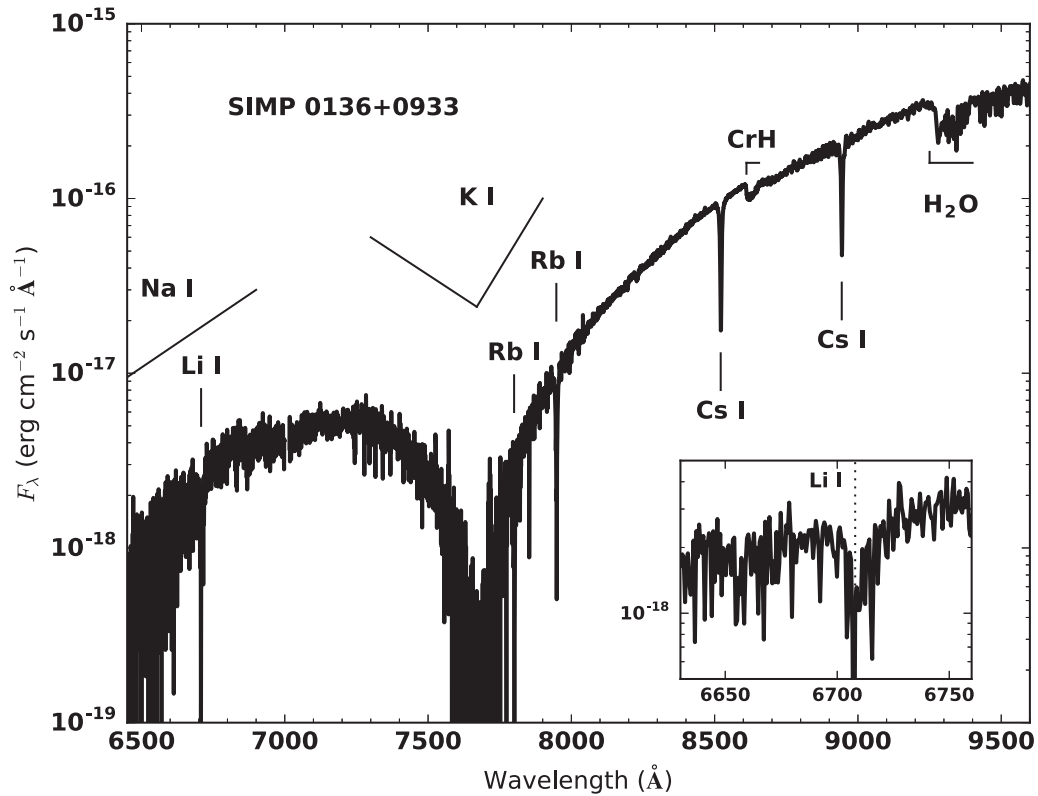

Figure 3. The DEIMOS spectrum of SIMP 0136+0933, a T2 brown dwarf. The figure indicates the location of prominent alkali absorption lines and molecular features that shape the optical spectra of T dwarfs and define the T dwarf optical spectral sequence. The inset shows the spectral region around the Li I line, which is clearly detected in this target—see Section 5.8.

+2553 for T9 (Kirkpatrick et al. 2011). To aid in the visual classification, we also convolved the DEIMOS spectra down to the same resolution as the optical standards using a Gaussian kernel. We verified the results of the convolution process by matching our convolved DEIMOS spectra to the literature spectra of the same targets matching the resolution of the standards (e.g., 2MASS 0559−1404). The new optical spectral types are included in the Table 1 alongside the near-IR spectral types from Burgasser et al. (2006b) or Kirkpatrick et al. (2011). We also show the spectra in Figures 1 and 2, with the important spectral features detailed closely in Figure 3.

Through this comparison we discovered that four of the spectra display features that are clearly between those of the T2 and T5 spectral standards. The morphology is best illustrated by the strength of the CrH absorption, Cs I lines, and the H_2O absorption. This last water feature is at wavelengths that are influenced by telluric absorption in our spectra, however, the astrophysical signal completely dominates (see B03). The objects PSO 247+03 and SDSS 0758+3247 showed slightly weaker CrH absorption relative to the T2 standard and slightly stronger H_2O absorption but not as strong as the T5 standard while maintaining strong Cs I absorption. Both of these brown dwarfs have NIR spectral types of T2. 2MASS 1750+1759 and WISEP 0819−0335 show no CrH absorption like the T5 standard but with slightly weaker H_2O and stronger Cs I lines. These two targets have NIR spectral types of T3.5 and T4, respectively. These targets fill the gap in spectral morphologies between T2 and T5, and we propose that PSO 247+03 and WISEP 0819−0335 be considered the optical spectral standards for T3 and T4, respectively. We plot the standards for the T dwarf optical spectral sequence in Figure 4. Using these standards, we also update the optical spectral types of
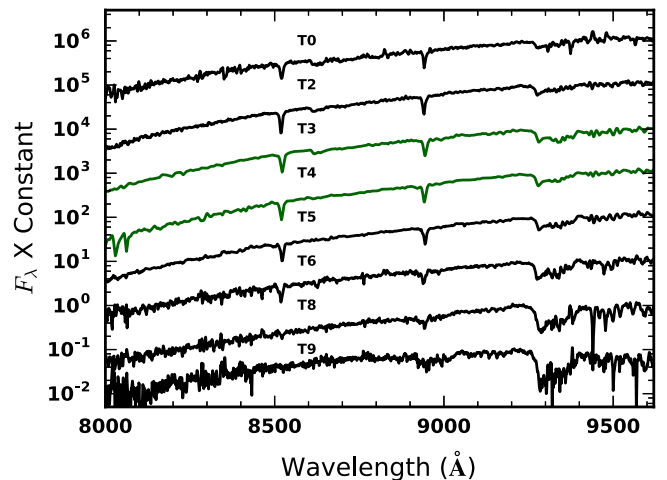

Figure 4. T dwarf optical spectral standards including our new additions for types T3 and T4. The T0 standard is from Kirkpatrick et al. (2008) and the T9 is from Kirkpatrick et al. (2011), while the rest are from B03. The T3 and T4 spectra have not been corrected for telluric absorption but have been convolved here to match the resolution of the literature standards.

SDSSp J102109.6−030419 and 2MASS 12095613−1004008 of T3.5 from Kirkpatrick et al. (2008) to T4.

3.2. Spectral Features

3.2.1. Alkali Lines

We measured the set of alkali absorption lines in our new spectra. These are the Cs I lines at 8521 and 8943 Å and the Rb I lines at 7800 and 7948 Å (K99). Following B03, to

measure the absorption strength of each line, we simultaneously fit a Lorentz distribution to the line profile and a linear continuum to the 120 Å region centered at the nominal wavelength position of each line. We used a maximum likelihood estimate and a MCMC routine implemented in `Python` to determine the best-fit parameters of the model (Patil et al. 2010). The likelihood was constructed from the product of the probability of each datum which was assumed to be described by a normal distribution centered at the measured flux for each wavelength with the standard deviation given by the error spectrum. The model is given as

$$S_\lambda = b + m(\lambda - \lambda_0) + \frac{A}{\pi} \frac{\gamma}{(\lambda - \lambda_0)^2 + \gamma^2}, \qquad (1)$$

where λ_0 is the center of the absorption line, A is the total flux absorbed by the line, γ defines the width of the Lorentz distribution, m is the slope of the continuum, and b is the level of the continuum at the center of the line. The pseudo-equivalent widths, pEWs, for each line are computed as

$$\mathrm{pEW} = A/b. \qquad (2)$$

Additionally, we compared the corresponding fit using a Voigt line profile (the convolution of a Lorentz profile with a Gaussian profile) to the Lorentz profile fits. Although the Gaussian component is typically dominant in the core, whereas the Lorentz profile dominates in the wings of the line from pressure broadening, we found that in all cases the fit using the Voigt line profile model tended to the Lorentz profile with little to no contribution from the Gaussian component. Gaussian line profile fits also did a poor job of fitting the data compared to the Lorentz profile. Additionally, there is a systematic bias in the measured pEWs depending on the assumed shape of the line profile. An assumed Gaussian profile yields lower pEWs than the corresponding fit using a Lorentz line profile with differences of up to 15%. These results signify the importance of pressure broadening in determining the shape of the absorption line profiles for these high gravity atmospheres.

We report the pEWs for our line profile fits in Table 2, where we include, in addition to 28 of the targets we observed from Table 1 (all except 2MASS 0036+1821), measurements for 3 of the 7 WISE T dwarfs (see Section 2.2.2) for which we could get decent line fits, and measurements for the L8, T0, and T6 optical standards (using the literature spectra). The T2 and T8 optical standards already have alkali line fitting measurements from B03. Not every line was visible in every spectrum due to the lower flux in the fainter parts of the spectrum. If a line was clearly identified, we fit the line profile as described above. If we detected the continuum but were not able to distinguish a clear absorption line, we determined a 3σ upper limit from the uncertainty in the continuum and the sum of the residuals in a 40 Å region around the line center after the linear continuum was subtracted. When there was no clear continuum we left the entry in Table 2 blank. All included, the table includes 34 distinct targets. In Figure 5, we plot the pEWs of the Cs I lines as a function of optical spectral type for the T dwarfs with black circles representing our new measurements and the gray squares representing literature data. The peak Cs I absorption across the T dwarf sequence occurs for mid T dwarf spectral types.

3.2.2. Spectral Ratios

We also examined the series of spectral ratios summarized by B03 in their Table 5, in particular Cs I(A), CrH(A), H₂0, and Color-e. The ratios measure the respective spectral features indicated, with Color-e corresponding to the overall spectral slope of the pseudo-continuum between 8450 and 9200 Å. Before measuring the features, we convolved down our DEIMOS spectra to the same resolution as their LRIS sample, as in Section 3.1, in order to compare their measurements with ours. We also used the line center measurements from the alkali line fitting (Section 3.2.1) to shift each spectrum to a consistent frame in line with the expected positions of the absorption features. The results are presented in Table 3, where we show measurements from 28 of our newly observed targets, all except 2MASS 0036+1821 for which the spectrum did not cover the selected spectral regions, plus the ratios measured for the 7 late T dwarfs in the the literature from WISE (see Section 2.2.2). We also plot the ratios as a function of optical spectral type in Figure 6, focusing on the T dwarf sequence with our newly expanded sample.

As demonstrated by B03, the ratio of the CrH(A) feature to the H₂O feature tracks the T dwarf optical spectral sequence most clearly (see Figure 6, top right). With our expanded data sample, we show that the relation is rather tight throughout the whole T dwarf optical sequence, despite the influence of weak telluric absorption in the H₂O index in our new data (See Section 3.1). A quadratic fit to the spectral types as a function of CrH(A)/H₂O yields a residual scatter that is less than one full spectral type. This particular ratio is the best predictor of the overall spectral morphology, whereas features like the overall optical slope or the alkali line depths show considerably more scatter. Moreover, this ratio combination continues smoothly across the L/T transition.

The H₂O feature, shown in the lower left of Figure 6 grows gradually through the optical spectral sequence before greatly increasing for spectral types after T8. Two of our targets with new optical spectra, 2MASS 1114−2618 and 2MASS 0939−2448, showed absorption in line with the T9 optical standard WISE 1741+2553 from Kirkpatrick et al. (2011). These spectra match the overall shape of the T8 standard, however the H₂O band is slightly stronger and agrees well with the T9 standard. Because the overall shape so closely matches the T8 standard, we retain the T8 optical spectral type for these objects, however, they likely represent a transition to cooler objects, T9s and even Y dwarfs. These remarks are in line with the results of Burgasser et al. (2006a), which determine that these two objects have effective temperatures cooler than the T8 standard with an upper limit of $T_{\mathrm{eff}} \lesssim 700$ K.

4. Hα ACTIVITY

Of particular interest in this study is the prevalence of Hα emission in late L dwarfs and T dwarfs. Most of the spectra did not show a clear indication of Hα emission, see Table 4. From our observations, only 2MASS 0036+1821, 2MASS 1750 −0016, SDSS 0423−0414, and 2MASS 1043+2225 had excess emission around the location of Hα. We plot the corresponding Hα profiles in Figures 7 and 8. To measure this flux we fit a line to the 40 Å region around the nominal location of the emission line, excluding the 6 Å region centered at 6563 Å. We subtracted the linear fit from the spectrum and summed the flux between 6560 and 6566 Å as the flux in the

Table 2
Alkali Line Pseudo-equivalent Widths

Object	Opt. Spectral Type	8521 Å Cs I		8943 Å Cs I[a]		7800 Å Rb I		7948 Å Rb I	
		λ_0 (Å)	pEW (Å)	λ_0 (Å)	pEW (Å)	λ_0 (Å)	pEW (Å)	λ_0 (Å)	pEW (Å)
2MASS 0700+3157	L3.5	8521.72 ± 0.02	3.64 ± 0.04	8943.98 ± 0.02	2.32 ± 0.04	7800.96 ± 0.03	4.62 ± 0.08	7948.38 ± 0.03	4.34 ± 0.06
2MASS 0835–0819	L5	8521.68 ± 0.01	4.72 ± 0.03	8943.903 ± 0.022	$2.56^{0.04}_{0.03}$	7800.79 ± 0.04	6.51 ± 0.11	7948.22 ± 0.02	6.18 ± 0.06
2MASS 1507-1627	L5	8520.42 ± 0.01	5.81 ± 0.03	8942.596 ± 0.014	3.41 ± 0.03	7799.76 ± 0.04	$9.01^{0.16}_{0.15}$	7947.01 ± 0.02	8.13 ± 0.07
2MASS 1750–0016	L5	8522.00 ± 0.01	5.84 ± 0.04	8944.21 ± 0.02	3.47 ± 0.04	7801.20 ± 0.05	$9.63^{0.20}_{0.19}$	7948.485 ± 0.025	$8.15^{0.09}_{0.08}$
SDSS 1416+1348	L6	8519.99 ± 0.01	6.43 ± 0.03	8942.07 ± 0.01	3.91 ± 0.03	7799.24 ± 0.06	11.11 ± 0.22	7946.54 ± 0.02	9.13 ± 0.08
WISE 1647+5632	L7	8521.6 ± 0.2	7.2 ± 0.5	8943.8 ± 0.3	4.2 ± 0.6	...	<42	7947 ± 2	12^{16}_{6}
SDSS 0423–0414	L7.5	8521.81 ± 0.02	7.84 ± 0.07	8943.86 ± 0.03	5.62 ± 0.06	7801.0 ± 0.2	$9.3^{0.7}_{0.6}$	7948.30 ± 0.07	9.22 ± 0.20
SDSS 1052+4422	L7.5	8521.96 ± 0.06	$6.82^{0.17}_{0.16}$	8944.27 ± 0.08	4.69 ± 0.16	...	<23	7948.7 ± 0.3	$8.6^{1.0}_{0.9}$
2MASS 1043+2225	L8	8520.68 ± 0.06	7.41 ± 0.18	8942.77 ± 0.07	$5.42^{0.16}_{0.15}$	...	...	7947.2 ± 0.3	9.6 ± 0.9
2MASS 1632+1904	L8	8520.7 ± 0.1	7.6 ± 0.3	8942.2 ± 0.3	5.5 ± 0.5	...	...	...	...
SDSS 0837–0000	T0	8520.5 ± 0.3	$9.0^{0.7}_{6}$	8942.5 ± 0.3	8.1 ± 0.7	...	...	...	...
SIMP 0136+0933	T2	8521.77 ± 0.02	9.70 ± 0.06	8943.969 ± 0.014	8.58 ± 0.04	7801.40 ± 0.27	$10.6^{1.2}_{1.1}$	7948.58 ± 0.12	9.96 ± 0.32
		8519.07 ± 0.02	10.16 ± 0.06	8941.35 ± 0.01	8.45 ± 0.04	7798.8 ± 0.6	14 ± 2	7945.81 ± 0.13	10.96 ± 0.38
WISE 0656+4205	T2	8520.52 ± 0.07	9.57 ± 0.23	8942.54 ± 0.05	8.45 ± 0.15	...	<56	7948 ± 1	12 ± 3
2MASS 2139+0220	T2	8518.75 ± 0.06	8.55 ± 0.17	8941.11 ± 0.05	7.39 ± 0.12	...	...	7944.2 ± 0.5	10 ± 1
SDSS 0758+3247	T3	8524.2 ± 0.3	$8.4^{0.9}_{0.8}$	8946.3 ± 0.2	7.4 ± 0.6	...	...	...	<37
PSO 247+03	T3	8522.18 ± 0.07	10.23 ± 0.23	8944.17 ± 0.06	8.45 ± 0.16	...	<41	7951^{2}_{1}	10^{5}_{3}
WISE 0819-0335	T4	8519.97 ± 0.12	8.97 ± 0.42	8942.00 ± 0.10	8.52 ± 0.26	...	<51	...	<33
2MASS 1209–1004	T4	8522.6 ± 0.3	12.2 ± 0.6	8945.4 ± 0.3	9.7 ± 0.5	...	...	...	<10
2MASS 1750+1759	T4	8521.1 ± 0.3	$11.7^{1.2}_{1.1}$	8942.95 ± 0.27	8.5 ± 0.7	...	...	...	<89
SDSS J0000+2554	T5	8521.48 ± 0.07	8.79 ± 0.23	8943.81 ± 0.06	8.38 ± 0.15	...	<48	7950^{2}_{1}	10^{10}_{3}
2MASS 0559–1404	T5	8521.565 ± 0.029	7.73 ± 0.10	8943.66 ± 0.02	7.48 ± 0.07	7800.1 ± 0.5	12^{3}_{2}	7948.15 ± 0.25	11.5 ± 0.7
SDSS 0926+5847	T5	8521.07 ± 0.15	9.2 ± 0.4	8943.6 ± 0.1	8.57 ± 0.25	...	<69	...	<32
WISE 1841+7000	T5	$8519. \pm 2.$	7^{4}_{3}	8942 ± 1.0	14^{4}_{3}	...	...	...	...
2MASS 2254+3123	T5	8521.29 ± 0.10	8.7 ± 0.3	8943.59 ± 0.07	8.26 ± 0.18	...	<108	...	<25
2MASS 0243-2453	T5.5	8521.5 ± 0.1	8.6 ± 0.4	8943.71 ± 0.10	8.88 ± 0.23	...	...	...	<41
2MASS 1754+1649	T5.5	8521.44 ± 0.17	$8.1^{0.6}_{0.5}$	8943.68 ± 0.15	8.64 ± 0.37	...	...	...	<69
2MASS 1231+0847	T6	8521.01 ± 0.13	7.1 ± 0.3	8942.93 ± 0.09	7.46 ± 0.21	...	<35	7946 ± 1	11 ± 3
WISE 1506+7027	T6	8522.19 ± 0.28	7.6 ± 0.8	8945.0 ± 0.3	7.9 ± 0.6	...	...	...	<40
SDSS 1624+0029	T6	8520.68 ± 0.10	$6.65^{0.28}_{0.27}$	8942.78 ± 0.09	7.18 ± 0.21	...	<44	7945^{1}_{2}	10^{3}_{3}
WISE 1019+6529	T7	...	<19	8944^{1}_{20}	5^{5}_{3}	...	...	...	...
WISE 2340–0745	T7	8519.9 ± 0.7	6 ± 1	8942.4 ± 0.5	7.4 ± 0.8	...	...	...	...
2MASS 0727+1710	T8	8521.2 ± 0.2	$5.13^{0.35}_{0.34}$	8943.43 ± 0.15	6.7 ± 0.3	...	<23	$7949.1^{0.5}_{0.6}$	8 ± 2
2MASS 0939-2448	T8	8521.7 ± 0.6	2.8 ± 0.5	...	...	...	...	...	<25
2MASS 1114-2618	T8	8523.1 ± 0.5	$4.7^{1.0}_{0.8}$	...	...	...	...	...	...

Note.

[a] For the L dwarfs the line is confused with a broader molecular absorption band. For the latest T dwarfs the line is obscured by CH_4 absorption.
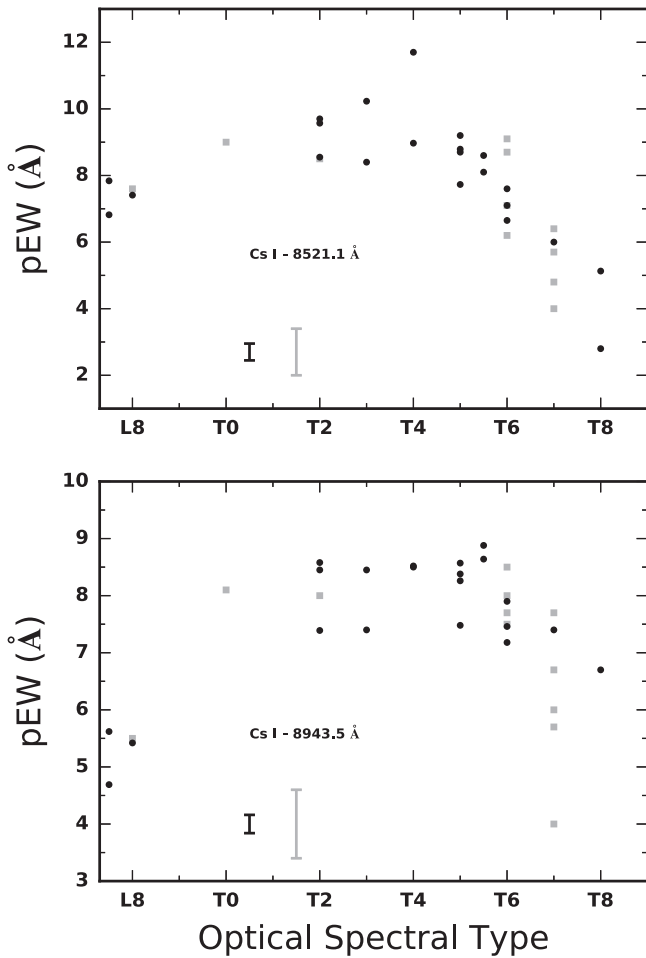
Figure 5. Measured pEWs of the Cs I absorption lines at 8521 Å (top) and 8943 Å (bottom) as a function of optical spectral type across the T dwarf sequence. We plotted the values listed in Table 2 (black circles), and also the literature measurements from B03 (gray squares), including new measurements for the L8 and T0 standards, 2MASS 1632+1904 and SDSS 0837−0000, respectively. We only plot the values with less than 20% uncertainties and include the median full errorbar length in the lower left of each plot. The absorption peaks for T2–T4 objects and declines in late T dwarfs. The scatter at a given spectral type is likely associated with differences in gravity and/or metallicity between the different brown dwarfs. The larger scatter for late T dwarfs in the Cs absorption line at 8943 Å has to do with the onset of a CH_4 band around the location of the Cs line.

emission line. The uncertainty was determined from the error spectrum for the sum of that region with the uncertainty in the continuum below the line added in quadrature. In Table 4, we report the flux measurements with the 1σ uncertainty level as well as the 3σ upper limits.

For these measurements we did not apply the line fitting procedure developed in Section 3.2.1 for a couple of reasons. First, This approach allowed us to compare our measurements to the values in the literature in a consistent way. Second, the line fitting assumes a particular shape for the line profile, which is justified for the absorption lines but not for these emission lines. We did attempt to fit example profiles, Gauss, Lorentz and Voigt, however one did not particularly outperform the others.

We calculated the ratio of the luminosity in Hα to the brown dwarf's bolometric luminosity, $L_{H\alpha}/L_{bol}$, by making use of new bolometric corrections from Filippazzo et al. (2015),

Table 3
Spectral Ratios[a]

Object	SpT Opt	CsA	H_2O	CrH/H_2O	Color-e
2MASS 0700+3157	L3.5	1.3	1.08	1.37	1.71
2MASS 0835−0819	L5	1.41	1.12	1.72	1.56
2MASS 1507−1627	L5	1.56	1.12	1.79	1.56
2MASS 1750−0016	L5	1.53	1.18	1.5	1.56
SDSS 1416+1348	L6	1.61	1.14	1.58	1.78
WISE 1647+5632	L7	1.63	1.29	1.1	1.72
SDSS 1052+4422	L7.5	1.65	1.23	0.98	2.45
SDSS 0423−0414	L7.5	1.77	1.24	1.2	2.02
2MASS 1043+2225	L8	1.66	1.28	0.95	2.16
SIMP 0136+0933	T2	2.3	1.39	0.752	4.06
WISE 0656+4205	T2	2.01	1.42	0.693	4.54
2MASS 2139+0220	T2	2.11	1.61	0.64	3.8
SDSS 0758+3247	T3	1.93	1.63	0.713	3.54
PSO 247+03	T3	2.03	1.65	0.648	3.87
WISE 0819−0335	T4	1.98	1.55	0.615	4.89
2MASS 1750+1759	T4	2.53	1.47	0.663	4.64
SDSS J0000+2554	T5	1.91	1.68	0.55	4.85
2MASS 0559−1404	T5	1.75	1.59	0.579	4.61
SDSS 0926+5847	T5	1.88	1.55	0.59	4.49
WISE 1841+7000	T5	1.87	1.88	0.429	4.87
2MASS 2254+3123	T5	1.84	1.55	0.607	4.9
2MASS 0243−2453	T5.5	1.83	2.17	0.409	5.26
2MASS 1754+1649	T5.5	1.84	2.16	0.412	5.57
2MASS 1231+0847	T6	1.58	2.14	0.42	4.42
WISE 1506+7027	T6	1.77	2.4	0.37	4.23
SDSS 1624+0029	T6	1.62	2.18	0.404	4.26
WISE 1019+6529	T7	2.05	2.57	0.447	4.57
WISE 2340−0745	T7	1.76	2.35	0.381	4.15
2MASS 0727+1710	T8	1.43	2.65	0.329	4.32
2MASS 0939−2448	T8	1.21	5.85	0.147	4.77
2MASS 1114−2618	T8	1.25	5.77	0.151	4.76
WISE 1457+5815	T8	1.47	2.55	0.364	3.62
WISE 1617+1807	T8	1.92	3.15	0.252	3.14
WISE 1653+4444	T8	1.16	2.11	0.408	4.17
WISE 1741+2553	T9	1.07	5.24	0.157	2.46

Note.
[a] The spectral ratios are ratios of the flux in the spectrum describing the strength of different spectral features, see Table 5 of B03 for definitions.
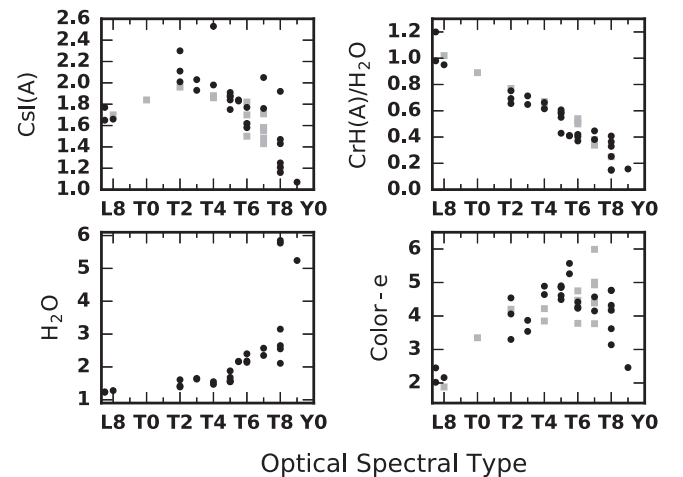

Figure 6. Spectral ratios of Table 3 as a function of optical spectral type. The black points are our new measurements and the gray squares comprise literature values from B03 and Kirkpatrick et al. (2008). We focus on the T dwarf sequence but show the points down to L7.5 to illustrate how the ratios change across the L/T transition. The CrH(A)/ H_2O ratio shows the clearest and tightest trend with spectral type.

Table 4
New Hα Measurements

Object	SpT Opt	f_α (10^{-18} erg s^{-1} cm^{-2})	$\log(L_{H\alpha}/L_{bol})$
2MASS 0036 +1821[a]	L3.5	...	−6.1
2MASS 0700+3157	L3.5	<15	<−6.4
2MASS 0835−0819	L5	<12	<−6.5
2MASS 1507−1627	L5	<17	<−6.5
2MASS 1750−0016	L5	21.4 ± 4.8	−6.2 ± 0.1
SDSS 1416+1348	L6	<18	<−6.6
WISE 1647+5632	L7	<4.6	<−5.6
SDSS 0423−0414	L7.5	16.3 ± 1.7	−5.9 ± 0.1
SDSS 1052+4422	L7.5	<4.7	<−5.8
2MASS 1043+2225	L8	4.7 ± 1.5	−5.8 ± 0.2
SIMP 0136+0933[b]	T2	<4.9	<−6.6
WISE 0656+4205	T2	<3.1	<−6.0
2MASS 2139+0220	T2	<4.8	<−6.0
SDSS 0758+3247	T3	<9.6	<−5.8
PSO 247+03	T3	<4.5	<−6.0
WISE 0819−0335	T4	<6.6	<−5.7
2MASS 1750+1759	T4	<13	<−5.0
SDSS J0000+2554	T5	<5.7	<−5.7
2MASS 0559−1404	T5	<5.1	<−6.3
SDSS 0926+5847	T5	<4.5	<−5.5
2MASS 2254+3123	T5	<4.8	<−5.8
2MASS 0243−2453	T5.5	<3.8	<−5.7
2MASS 1754+1649	T5.5	<5.1	<−5.4
2MASS 1231+0847	T6	<8.4	<−5.3
WISE 1506+7027	T6	<5.8	<−6.0
SDSS 1624+0029	T6	<4.0	<−5.7
2MASS 0727+1710	T8	<4.2	<−5.7
2MASS 0939−2448	T8	<2.8	<−5.8
2MASS 1114−2618	T8	<6.8	<−5.4

Notes.
[a] The value of $L_{H\alpha}/L_{bol}$ for 2MASS 0036+18 was determined using the measured EW and a χ value 1.415×10^{-6} from (Schmidt et al. 2014), taking the averages for the median χ of spectral types L3 and L4.
[b] The value listed for this object is only from the DEIMOS spectrum taken on 2014 December 22.

which uses the newly defined absolute magnitude scale ($M_\odot = +4.74$).[9] We use the *J*-band bolometric correction as a function of spectral type to determine the bolometric luminosity since it has the least amount of scatter for the field T dwarfs (Filippazzo et al. 2015). The values of $L_{H\alpha}/L_{bol}$ for our observations are also listed in Table 4. We have also compiled the literature measurements from Burgasser et al. (2000a, 2002b), and B03, and report them in Table 5, with updated values of $L_{H\alpha}/L_{bol}$ based on the new bolometric corrections. For three of the objects with literature measurements shown in Table 5, we took new spectra in our current survey with Hα measurements shown in Table 4: 2MASS 0559 −1404, SDSS 1624+0029, and 2MASS 0727+1710. Table 5 also includes flux measurements for SDSSp J083717.22 –000018.3, SDSSp J102109.6–030419, and 2MASS J12095613–1004008, based on archival spectra, which we reanalyzed to provide new limits on the Hα flux.

In Figure 9, we plot $L_{H\alpha}/L_{bol}$ as a function of optical spectral type. Measurements in Tables 4 and 5 are plotted as red filled circles with new limits as black downward triangles and limits from the literature as gray downward triangles. In the instances

---

[9] The new bolometric corrections are consistent with previous efforts by Liu et al. (2010).
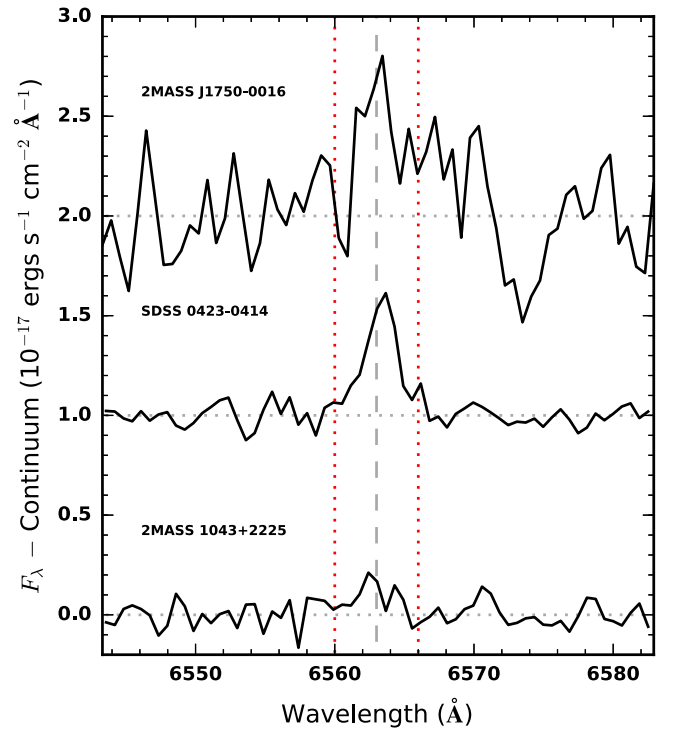

Figure 7. Zoom in of the region around the 6563 Å Hα emission line (vertical dashed line) for the spectra of 2MASS J1750−0016, SDSS 0423−0414, and 2MASS 1043+2225. The spectra have the local continuum subtracted and are offset by a constant for clarity with the line center marked by a dashed line. The vertical dotted lines delineate the region used to sum the Hα flux. We report the measurements of these fluxes in Table 4.
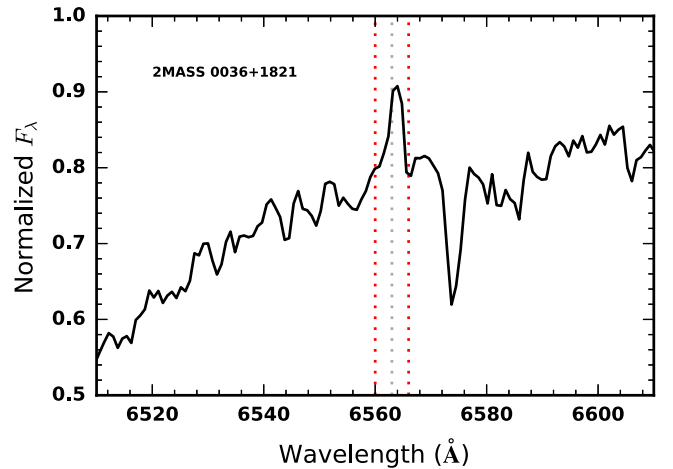

Figure 8. Normalized spectrum of 2MASS 0036+1821 in the region around Hα. The dashed line marks the expected position of the emission line and the dotted lines denote the region used to add up the emission line flux once the continuum has been subtracted. Unlike the observations for the targets in Figure 7, the spectrum for 2MASS 0036+1821 was not flux calibrated.

in which there were multiple measurements for a single target, either from our observations or in the literature, we plotted a detection, if available, or the most stringent limit for the non-detections. For comparison with earlier spectral types, we have also included measurements (blue squares) and limits (gray tri-symbols) compiled by Schmidt et al. (2015) and supplemented by Burgasser et al. (2015). These values include measurements from K99, Kirkpatrick et al. (2000), Hall (2002), Liebert et al. (2003), Schmidt et al. (2007, 2015), Reiners & Basri (2008),

Table 5
Literature T Dwarf Hα Emission[a]

Object	SpT Opt	f_α (10^{-18} erg s^{-1} cm^{-2})	$\log(L_{H\alpha}/L_{bol})$
SDSS 0837−0000[b]	T0	<4.4	<5.3
SDSS1254−0122	T2	7.5 ± 2.5	−5.9 ± 0.2
SDSS 1021−0304[b,c]	T4	<8.3	<−5.3
2MASS 1209 −1004[b,c]	T4	<1.7	<−6.1
2MASS 0559−1404	T5	<6.1	<−6.2
2MASS 0755+2212	T6	<12	<−5.1
2MASS 1225−2739	T6	<6.7	<−5.5
2MASS 1503+2525	T6	<9.6	<−5.9
2MASS 1534−2952	T6	<17	<−5.3
SDSS 1624+0029	T6	<4	<−5.7
2MASS 0937+2931	T7	<3.9	<−6.2
2MASS 1047+2124	T7	5.9 ± 2.7	−5.5 ± 0.2
2MASS 1217−0311	T7	<7.7	<−5.4
2MASS 1237 +6526[d]	T7	74.4 ± 0.8	−4.2 ± 0.1
SDSS 1346−0031	T7	<7	<−5.2
GL570D	T7	<6.5	<−5.6
2MASS 0415−0935	T8	<7.9	<−5.5
2MASS 0727+1710	T8	<3.6	<−5.9

Notes.
[a] Unless otherwise noted, flux measurements are from Burgasser et al. (2000a) or B03.
[b] Flux values are newly determined from archival spectra.
[c] Optical Spectral types are from this paper, updating values presented in Kirkpatrick et al. (2008).
[d] We report the average for this source taken from Burgasser et al. (2002b).

and Burgasser et al. (2011). We do not distinguish binaries in this plot, but note that for those objects, the optical spectrum is dominated by the warmer component and thus the points are representative of the position corresponding to the primary.

In Figure 10, we plot the fraction of objects shown in Figure 9 that have Hα detections as a function of optical spectral type from L dwarfs through to T dwarfs. Since the data comes from a variety of sources and surveys with different sensitivity limits there are observational biases inherent to this detection fraction. Additionally, many brown dwarfs have been demonstrated to exhibit variability in their Hα emission, potentially from rotation (Berger et al. 2009; Hallinan et al. 2015) or longer timescales (see Section 5.1). Thus, objects with only non-detections may yet display emission from further monitoring and/or more sensitive observations, so the detection fractions of Figure 10 are systematically low. With these caveats, our extended brown dwarf sample allows us to assess the prevalence of the Hα emission, going from L dwarfs to T dwarfs. The data in Figure 10 demonstrates that the declining prevalence of Hα emission, demonstrated for early-to-mid L dwarfs in Schmidt et al. (2015), declines to a low level by L4/L5 spectral types and is consistent with this low level through to late T dwarfs. Although the complete sample presented here does not have the virtue of a consistent detection threshold, as the subsample analyzed by Schmidt et al. (2015) does for the L dwarf activity fractions, putting everything together allows for a straightforward comparison between the T dwarfs and the L dwarfs.

It is clear that the number of objects with Hα emission for spectral types later than about mid-L is low. For all of the L dwarfs in this compilation, 67/195, $34^{+3.5}_{-3.2}$%, show Hα

emission. This detection fraction, however, is skewed by the high number of active early L dwarfs. For mid-to-late L dwarfs (L4–L8), only 7/75, $9.3^{+4.5}_{-2.4}$%, show Hα emission. For comparison, despite nearly doubling the number of measurements available in the literature for T dwarfs, our results show that most T dwarfs show no emission or very weak emission. Only 3/34, $8.8^{+7.4}_{-2.8}$%, distinct systems with T dwarf optical spectral types show Hα emission (see Tables 4 and 5). Luhman 16B, the nearby T dwarf, also has an EW limit, EW <1.5 Å, but no flux limit, so we did not include it in Table 5 (Faherty et al. 2014). Additionally, the 7 WISE T dwarfs with optical spectra from Kirkpatrick et al. (2011), but no flux measurements, also do not show any indication of Hα emission. Inclusion of these targets leads to the statistic that only 3/42, $7.1^{+6.2}_{-2.2}$%, of T dwarf systems show this emission feature. Given the broad similarities between the Hα detections of T dwarfs and late L dwarfs, we can also group them together to get an overall detection fraction for optical spectral types L4–T8 of 10/109, $9.2^{+3.5}_{-2.1}$%. Inclusion of the additional 8 T dwarfs without flux limits gives, for L4–T9, a detection rate of 10/117, $8.5^{+3.3}_{-1.9}$%. Since, we do not treat binaries separately, these figures could even decrease when accounting for each component in multiple systems.

Interestingly, these detection rates for late L dwarfs and T dwarfs are comparable to the total detection rate, ~7%, in surveys looking for brown dwarf radio emission in objects ⩾L6 (Kao et al. 2016; Lynch et al. 2016). If auroral processes are the dominant mechanisms responsible for magnetic emission in late L dwarfs and T dwarfs, these results suggest that geometric beaming of the radio emission is potentially totally absent or may not significantly affect the auroral detection rates.

5. INTERESTING INDIVIDUAL OBJECTS

5.1. 2MASS 0036+1821

This target is one of the few L dwarfs to exhibit detectable quiescent radio emission, as well as periodic highly polarized radio pulses (Berger 2002; Berger et al. 2005; Hallinan et al. 2008; McLean et al. 2012). Consequently, there have been numerous studies examining the magnetic activity of this object, looking for X-ray, radio and Hα emission (Berger et al. 2005; Hallinan et al. 2008; Reiners & Basri 2008). Previous studies in the optical report limits on the Hα emission of EW < 0.5 Å and <1.0 Å from Kirkpatrick et al. (2000) and Reiners & Basri (2008), respectively. The most stringent previous limit comes from a 4 hr monitoring observation by Berger et al. (2005) in which they do not detect anything to a limit of $\log(L_{H\alpha}/L_{bol}) \lesssim -6.7$. As the only radio pulsing brown dwarf to not show Hα emission, we decided to observe it further due to the potential association of the radio emission to Hα emission. Our new observations on 2012 July 19 (UT), clearly show an emission feature at 6563 Å with EW = 0.59 ± 0.08 and $\log(L_{H\alpha}/L_{bol}) = -6.1$ (see Figure 8). Since our spectrum of 2MASS 0036+1821 was not flux calibrated, we did not measure the flux of Hα emission, instead, we used the revised χ factors of Schmidt et al. (2014) to convert the measured EW to $\log(L_{H\alpha}/L_{bol})$. This measurement is in line with some of the previous limits, however, the detection greatly exceeds the limit placed by Berger et al. (2005). Although many L dwarfs have been shown to exhibit variable Hα emission, as evidenced in the compilation by Schmidt et al. (2015), the emission is generally not as weak as
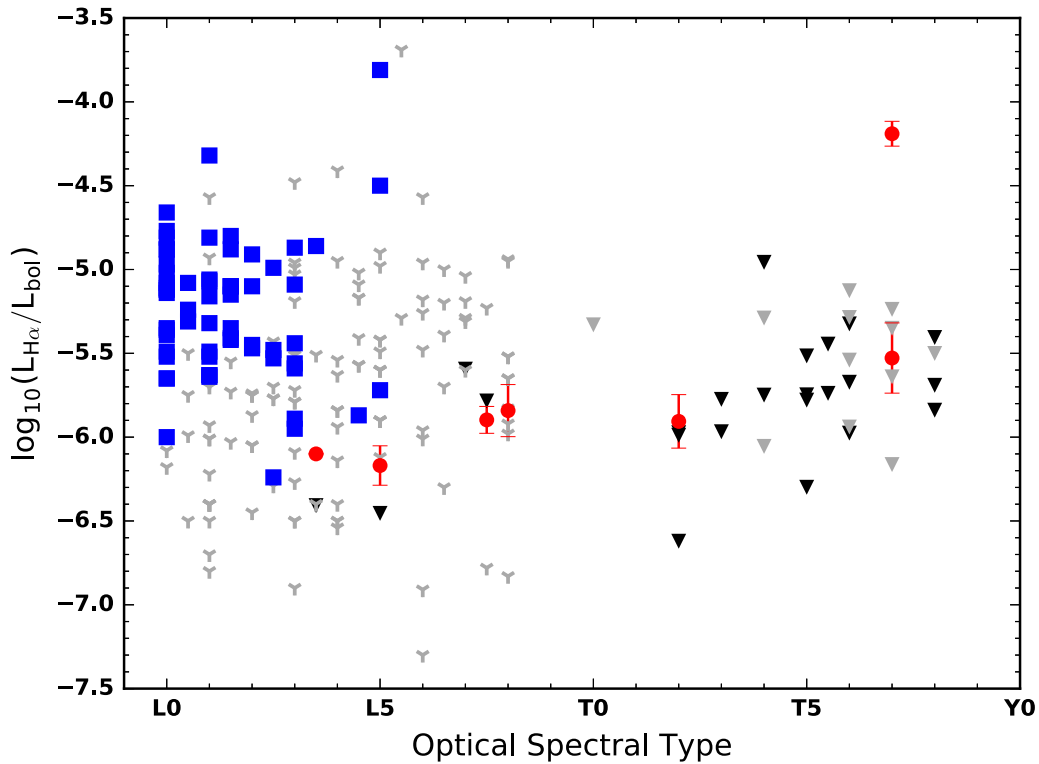
Figure 9. Logarithm of the luminosity in Hα relative to an object's bolometric luminosity as a function of optical spectral type. The red points mark measurements listed in Tables 4 and 5. Downward triangles mark the upper limits of the same tables with the darker points corresponding to new measurements from this paper and the lighter ones to previous studies of T dwarfs from Burgasser et al. (2000a) and B03. Literature values for L dwarf emissions as compiled by Schmidt et al. (2015) and supplemented by new measurements from Burgasser et al. (2015) are included as squares and tri symbols, respectively, for measurements and upper limits.
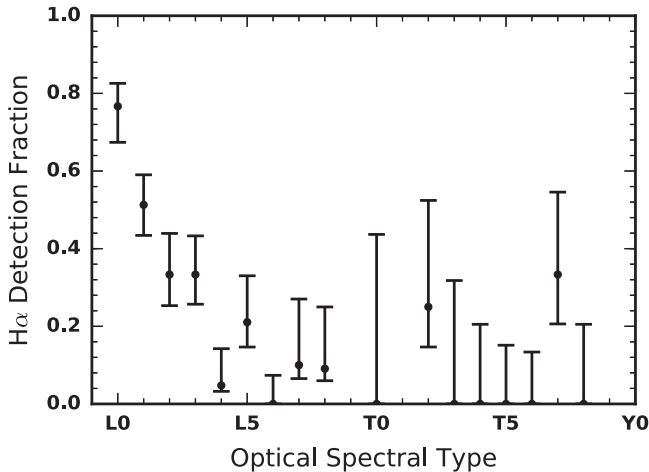
Figure 10. Detection fraction of objects as a function of optical spectral type from L dwarfs to T dwarfs based on the compilations by Schmidt et al. (2015), Burgasser et al. (2015), and this paper. Half spectral types have been rounded down to earlier spectral types and the errorbars represent the 68% confidence interval of the corresponding binomial distribution. At spectral types later than about L4/L5, the prevalence of Hα detections is low.

we have detected for 2MASS 0036+1821, nor have most of these targets been monitored over their full rotational periods. Thus, the intermittent variability that we are detecting, at timescales definitively exceeding the rotational period, represents a new phenomena.

To explain their observed radio emission, Berger et al. (2005) considered the possibility that it could be the result of

enhanced activity due to a tidal interaction with a close in companion which orbits on a timescale consistent with the 3 hr period in their data. More recent results, however, positively attribute the radio emission to the ECMI and the periodic signature to a combination of the brown dwarf's rotation and the beaming effect of the emission mechanism (Hallinan et al. 2008). Additionally, the new Hα emission suggests the presence of long-term variability to the magnetic processes.

In the context of auroral radio emission and its potential connection to Hα emission, the intermittent variability of this object can be coherently explained via a potential flux tube interaction between the brown dwarf and a satellite, whose orbit modulates the long-term Hα emission. Energetic electrons moving along the field lines are responsible for the radio pulses and generate the Hα emission when they precipitate into the atmosphere and deposit their energy at the flux tube footpoint. This scenario is analogous to the interaction between Jupiter and its moon Io (e.g., Vasavada et al. 1999). For this scenario to be consistent with the data, the satellite must orbit with a period $\gtrsim$8 hr, or else the monitoring campaign of Berger et al. (2005) should have seen some indication of Hα emission.

The presence of a potential companion is also consistent with the inclination, i, of this system. Crossfield (2014) report a $v \sin i$ of $40.0 \pm 2.0\,\mathrm{km\,s^{-1}}$, which is a weighted average of the consistent measurements from Jones et al. (2005), Zapatero Osorio et al. (2006), and Reiners & Basri (2008). Early efforts to understand the magnetic emission from 2MASS 0036+1821 were confounded by the low $v \sin i = 15 \pm 5\,\mathrm{km\,s^{-1}}$ measurement from Schweitzer et al. (2001). However, Reiners & Basri (2008) attributed that outlying value to mismatches between the observed spectra and the atmospheric models used by

Schweitzer et al. ([2001](#)). Using a rotational period of 3.08 hr, $v \sin i$ of 40 km s^{-1} and a radii range between $0.9 R_{\mathrm{Jup}}$ and $1 R_{\mathrm{Jup}}$, for this field brown dwarf, gives the range of inclinations, $i \sim 80°–90°$ (Hallinan et al. [2008](#)). During the course of the satellite's orbital evolution, the corresponding flux tube footpoint, the location of the Hα emission, traces a path around the magnetic axis of the brown dwarf. Since the magnetic axis is not likely to be very misaligned with the rotational axis (for example, Jupiter's magnetic axis differs by only ∼10° from its rotational axis Badman et al. [2015](#)), and since the brown dwarf has a high inclination, it is very plausible that a hidden satellite could be modulating the Hα for this target, the emission being visible during certain orbital phases but hidden on the opposite face of the brown dwarf during others.

Depending on its orbital semimajor axis and orbital inclination, there is a possibility that such a satellite could be transiting the system. For example, an Earth sized satellite around a Jupiter sized brown dwarf would produce a transit depth of $\delta = (R_{\oplus}/R_{\mathrm{Jup}})^2 = 0.008$. Photometric monitoring from the ground by Harding et al. ([2013](#)) detected rotational variability in two 5 hr observations in I-band observations of 2MASS 0036 +1821 with 1% photometric precision, however they did not see any transits. *Spitzer* monitoring with 0.1% photometric precision also detected variability but no transits in their 14 hr observation (Metchev et al. [2015](#)). These observing campaigns could have missed the transit for a longer period satellite, or the object may not be transiting at all. By comparison, Io orbits Jupiter with an 1.77 day period. If an Earth sized planet is placed in a 1.77 day orbit around a 50 M_{Jup} brown dwarf of radius R_{Jup}, it would orbit at a distance of about 22 R_{Jup}. The plane of the orbit would need to be inclined at an angle, i_p, such that the $\cos i_p < (R_{\star} + R_p)/r$, for the planet to transit (for $i_p = 0$, the plane of the orbit coincides with the plane of the sky, face on; Winn [2010](#)). Using these orbital parameters gives an inclination of $i_p > 87°.1$; assuming that all orbital inclination are equally likely gives such a satellite a 3% probability of transiting. If the orbital inclination is consistent with the rotation axis, as it is in many exoplanetary systems, the chances of transiting are much higher Morton & Winn ([2014](#)). The current data is suggestive, but more extensive monitoring is required to confirm whether a satellite body is responsible for the long-term modulation of the Hα emission.

5.2. J1750−0016

2MASS 1750−0016 is a L5.5 dwarf discovered by Kendall et al. ([2007](#)). Only recently was this target observed at optical wavelengths by Burgasser et al. ([2015](#)) and they place an Hα EW emission limit of <0.4 Å. On the other hand, we detect excess emission at the location of Hα in our DEIMOS spectrum of this target and measure an emission strength of EW = 0.46 ± 0.10 Å (see Figure [7](#) and Table [4](#)). Although this emission is rather weak, Burgasser et al. ([2015](#)) report detections of a similar level in some of the other targets in their sample. Our new findings suggest that this target could have variable Hα emission like 2MASS 0036+1821 or many of the variable targets compiled by Schmidt et al. ([2015](#)).

5.3. SDSS 0423−0414AB

This target was revealed to be a binary system by Burgasser et al. ([2005](#)) in *Hubble Space Telescope* (*HST*) NICMOS imaging, with a L6 primary and T2 secondary. The target also showed strong Hα emission, with EW = 3 Å, and strong Li I absorption, with EW = 11 Å (Kirkpatrick et al. [2008](#)). We used our new DEIMOS observations to once again measure these features, looking for indications of variability. We measured the Hα emission, as described in Section [4](#), to be EW = 2.95 ± 0.30. This value is consistent with the values reported in the literature, suggesting that the emission may be steady across several year timescales.

We also compared the different measurements of the Li I absorption. We applied the alkali line fitting from Section [3.2.1](#) to both our new DEIMOS spectrum and the previous LRIS spectrum from Kirkpatrick et al. ([2008](#)). Both spectra yielded consistent results, however they were systematically higher than the reported values in the literature. This is likely due to the fact that the Lorentz line profile includes absorption in the wings of the distribution that may not be included by simply subtracting a continuum and adding up the flux in a predefined region around the line center. For consistency with the literature, we report an EW = 11.1 ± 0.4, in line with the literature value.

5.4. SDSS 1052+4422

This target had been designated as an early T dwarf (T0.5) by Chiu et al. ([2006](#)) in their discovery paper, based on the NIR spectrum. However, Dupuy et al. ([2015](#)) showed that SDSS 1052+4422 is actually a binary system from adaptive optics imaging. Their detailed study was able to determine dynamical masses of each component based on astrometric monitoring (Dupuy et al. [2015](#)). They also decomposed the composite NIR spectrum from the IRTF/SpeX library and determine spectral types of L6.5 ± 1.5 and T1.5 ± 1.0 (Dupuy et al. [2015](#)). Our new integrated light optical spectrum of this target fit between the L7 and L8 optical standards, and we assigned it a spectral type of L7.5. Our observations are thus consistent with the binary decomposition of L6.5 and T1.5, and provide further constraints on the properties of these objects. Binary systems like these, straddling the L/T transition, are important benchmarks for understand the evolution of brown dwarfs. For a given system, a large discrepancy between the NIR integrated light spectral type and the optical integrated light spectral type can be used as an indicator of a potential binary. This highlights the ability of optical spectra, as a counterpart to the NIR spectra, to be a useful diagnostic in verifying binary systems (see also Manjavacas et al. [2016](#)).

5.5. 2MASS 1043+2225

2MASS 1043+2225 is a late L dwarf reported by C07 to have tentative indications of Hα emission. Although, they see excess flux at the location of Hα, their results were inconclusive. Our new observations of this target confirm that this object does indeed exhibit weak Hα emission at a level of $\log(L_{\mathrm{H}\alpha}/L_{\mathrm{bol}}) = -5.8 \pm 0.2$ (see Table [4](#)). The detection is only just at the 3.1σ level, very similar to the weak detections of 2MASS 1047+2124 and 2MASS 1254−0122 from B03. We show the spectrum of this target around the Hα line in Figure [7](#).

For this object, we also report a tentative detection of Li I at 6708 Å. In Figure [11](#), we show this region of the spectrum alongside the the spectrum of C07, taken from the Ultracool RIZzo Spectral Library. We measured the absorption to have an EW = 10 ± 3 Å, in line with the typical EW of L8 dwarfs with Li I detections (Kirkpatrick et al. [2008](#)). Our more recent,
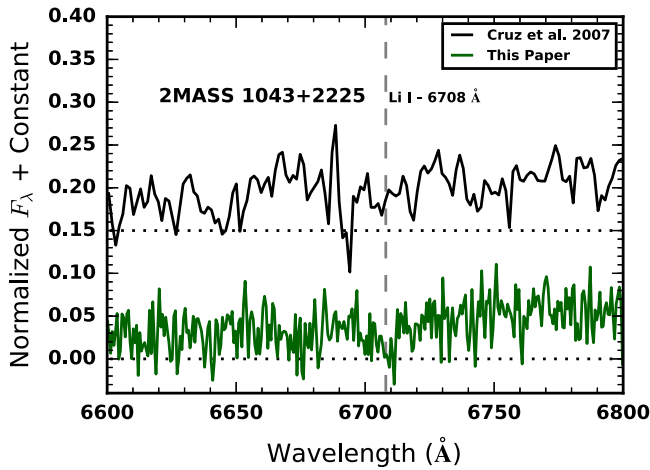
Figure 11. Spectra of 2MASS 1043+2225 zoomed in around the location of the Li I line at 6708 Å, showing both the spectrum from C07 (top; from the Ultracool RIZzo Spectral Library) and our DEIMOS spectrum (bottom). Our new spectrum shows a dip in the observed flux that could be Li I absorption, however, the previous spectrum from C07 only shows a small trough, in line with the continuum noise. We consider the corresponding lithium detection for this target as tentative.

higher resolution, observation shows that there may be an absorption feature there, however, the earlier spectrum does not. We consider this to be a tentative detection which will require deeper observations to confirm. If the absorption is real, this target would be added to the few very late L dwarfs and T dwarfs to display this important physical indicator of mass and age.

5.6. WISE 1647+5632

This target is included in the *WISE* discoveries from Kirkpatrick et al. (2011) and has a preliminary parallax placing it within 10 pc of the Sun. Kirkpatrick et al. (2011) assigned this object a NIR spectral type of L9 peculiar from an IRTF/SpeX spectrum, noting the discrepancies at H and K band between the spectrum and the standards. They added this object to a collection of unusually red L dwarfs. However, our optical spectrum of this target matches the L7 standard very well (see Figure 12). Our findings suggest that WISE 1647+5632 is likely an unresolved binary system straddling the L/T transition.

5.7. 2MASS 2139+0220

This target is one of the prominent T dwarfs with high amplitude variability in the J band, displaying up to 26% variability (Radigan et al. 2012). We included it in the sample to investigate if there could be any connection between the magnetic emissions and the cloud phenomena. We did not find any Hα emission and report an emission upper limit of EW < 8 Å. There have also been some suggestions that this object could be a binary due to its somewhat peculiar NIR spectrum (Bardalez Gagliuffi et al. 2014). Our observed spectrum matches the T2 optical spectral standard very well. This corroborates findings by Manjavacas et al. (2016) which rule out this scenario. The peculiar spectrum is thus, likely a consequence of a patchy atmosphere and the impact of cloud variability on the emergent spectral flux.
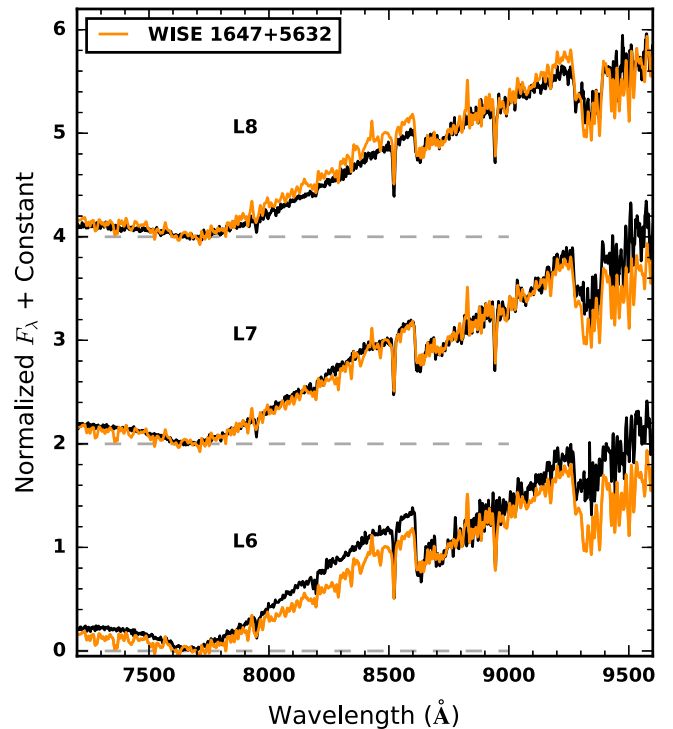
Figure 12. Comparison of the DEIMOS spectrum of WISE 1647+5632 (orange) against the optical standards for spectral types L6–L8 (black). The best match is produced by the L7 standard. This spectral type differs greatly from the NIR spectral type of L9p, and suggests that this target may be an unresolved binary (see Section 5.6).

5.8. SIMP 0136+0933

SIMP 0136+0933 is one of the archetypes for cloud variability at the L/T transition; it was found to exhibit 50 mmag photometric variability in J band and has since been followed up throughout the IR to characterize the patchy cloud structures of its atmosphere (Artigau et al. 2009; Apai et al. 2013; Radigan et al. 2014). As a potentially very interesting object in the context of auroral activity, we observed it with LRIS on 2014 August 27, and again with DEIMOS on 2014 December 22. In the first epoch we took two consecutive 1200s exposures, whereas in the second epoch we took two exposures of 1800s each, separated by 1.5 hr.

In no exposure did we detect any excess flux at the location of the Hα line. We measured stringent limits on the corresponding emission line flux of SIMP 0136+0933 from the co-added DEIMOS spectrum (see Table 4). Because we detect the underlying continuum in the combined spectra, for this target, we also report EW emission limits of <3.2 and <3.5 Å for the August and December nights, respectively. In the context of auroral emission, which may be rotationally modulated, the 1.5 hr of separation between the exposures in December correspond to a phase shift of 0.63, using the photometric rotational period of 2.39 hr (Apai et al. 2013). Although, it remains possible that we missed potential optical auroral emission from this source, the series of observations at different phases suggests that it may indeed lack Hα emission.

Our high signal-to-noise ratio spectrum, S/N ~ 6 at 6800 Å and S/N ~ 96 at 8600 Å, of SIMP 0136+0933 also allowed us to look for the presence of Li at 6708 Å. We plot this spectrum in Figure 3 with the inset zoomed in on the location of the Li I absorption. It is clearly present. We fit the
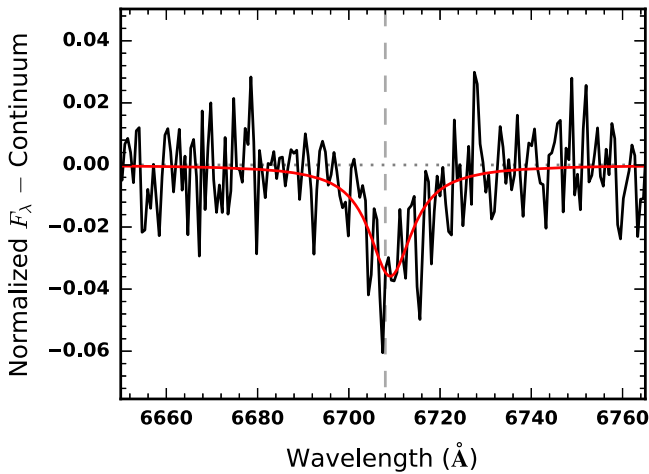
Figure 13. Spectrum of SIMP 0136+0933 around the Li I line at 6708 Å. The spectrum is normalized with the continuum profile subtracted. The line corresponds to a Lorentz line profile model fit of the data (see Section 3.2.1).

Figure 14. Cs I absorption lines of SIMP 0136+0933 between the observations in August and December plotted as solid lines and the Lorentz line profile model fits plotted as dashed lines. The pEWs of the lines are significantly different and likely reflect spectroscopy variability between the two observations for this photometrically variable target, see Section 5.8.

absorption line as we fit the other alkali lines in Section 3.2.1 with a Lorentz line profile and over-plotted the model result in Figure 13. As in the case of SDSS 0423–0414, we report EW values not based on the fit but a simple summation of the absorption line region (see Section 5.3). We measure EW values of 6.6 ± 1.0 and 7.8 ± 1.0 Å for the August and December observations, respectively. SIMP 0136+0933 joins the T0.5 dwarf, Luhman 16B (EW = 3.8 ± 0.4), as the second T dwarf and the latest spectral type object with a clear lithium detection in its atmosphere (Faherty et al. 2014). Although the spread of the values between the two objects is in line with the spread of detections for L8 dwarfs from Kirkpatrick et al. (2008), this absorption appears to be particularly strong by comparison given that SIMP 0136+0933 has a later spectral type and possibly cooler atmosphere.[10] As Lodders (1999) discussed, the Li I in the atmosphere becomes readily depleted by the formation of LiCl gas and other Li bearing substances like LiOH in cool dwarf atmosphere below temperatures of about 1600 K. Kirkpatrick et al. (2008) showed that the peak of Li I absorption takes place around a spectral type of L6.5 and declines for later spectral types.

Thus, the strong Li I of SIMP 0136+0933 is somewhat anomalous, however it is interesting to note that in addition to SIMP 0136+0933, Luhman 16B also exhibits cloud variability (Burgasser et al. 2014; Crossfield et al. 2014). The presence of Li may be related to the transition from L to T spectral types within a patchy cloud atmosphere.[11] Indeed, although our Li I EW measurements from the different epochs are formally in agreement within the 2σ level, the central values differ by 15%. If this is due to cloud phenomena in the atmosphere, the spectra from the different epochs could be dominated by flux from atmospheric levels with differing Li I depletion.

The two different epochs did allow us to observe spectroscopic variability in the other optical absorption lines. We note
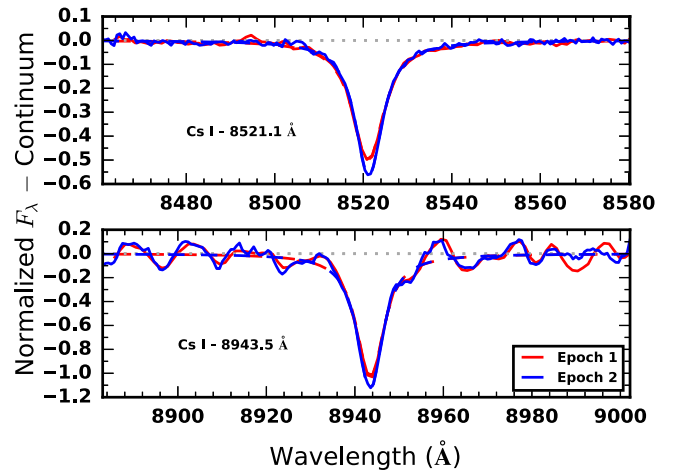
that the difference of the pEWs in the co-added spectra from the two epochs, for the lines reported in Table 2, are statistically significant. This is especially true of the Cs I lines where the S/N is greatest. For the first epoch, 2014 August 27, we measured pEWs of 10.16 ± 0.06 Å and 8.45 ± 0.04 for the Cs I lines at 8521 Å and 8943 Å, respectively. For the second epoch, 2014 December 22, we measured pEWs of 9.70 ± 0.06 Å and 8.58 ± 0.04 for the same lines, respectively. The difference between the pEW measurements for the Cs I line at 8521 Å is different from 0 at the 5.4σ level and similarly at the 2.3σ level for the Cs I line at 8943 Å. The Rb I lines at 7948 Å were measured to have pEWs of 10.96 ± 0.38 Å and 9.96 ± 0.32 Å for epoch 1 and epoch 2, respectively, yielding a difference that is significant at the 2σ level. In Figure 14, we plot a comparison of these spectral line profiles with the continuum subtracted and the corresponding Lorentz profile model fits (see Section 3.2.1).

The pEW measurements track the changes in the absorption relative to the nearby pseudo-continuum. The two different Cs I line observations did not show the same degree of variation, suggesting that this variability may be driven as much by differences in the relative continuum in the different parts of the spectrum as in the individual absorption line strength. These results provide support for the interpretation of cloud variability in the atmosphere of this object and supports the idea that there could be significant optical variability to coincide with the large-amplitude NIR variability, potentially even in the Li I absorption. In fact, Heinze et al. (2015) showed that photometric optical variability in brown dwarfs could be stronger than the NIR variability and Buenzli et al. (2015) used *HST* grism observations to demonstrate spectroscopic variability from 0.8 to 1.15 μm in both components of Luhman16AB.

6. DISCUSSION AND SUMMARY

We have conducted a new survey at red optical wavelengths (6300–9700 Å) looking for Hα emission in a large sample of late L dwarfs and T dwarfs. We acquired new optical spectra for 18 targets without previous spectra and several additional

---

[10] Disentangling the effective temperature, gravity and cloud effects remains a challenging problem in brown dwarf atmospheric modeling and depending on the different assumptions can yield differing answers, even when good data are available (Marley et al. 2010; Apai et al. 2013; Faherty et al. 2014; Marley & Robinson 2015).

[11] We did not see any indication of Li I in our LRIS spectrum of 2MASS 2139 +0220, however, there was not enough signal in the continuum to definitively rule it out.

spectra looking for potential variability in the emission features. We have nearly doubled the number of red optical spectra available for T dwarfs and used our new observations, in conjunction with available spectra, to examine prominent spectral features and the optical T dwarf sequence.

Our findings include two objects that fill the gap between the T dwarf optical spectral standards from T2 to T5. We proposed PSO 247+03 as the T3 spectral standard and WISE 0819−0335 as the T4 spectral standard. These two targets are relatively bright and are both near the equatorial plane, allowing for observational access from both the northern and southern hemispheres.

We also observed Li I absorption at 6708 Å in the spectrum of SIMP 0136+0933, one of the most prominent IR photometric variable brown dwarfs. This object becomes only the second T dwarf and the latest type object to display this feature. We also see spectroscopic variability in the strength of the absorption lines that is likely related to the heterogeneous cloud phenomena present in the atmosphere.

Our survey included new Hα detections for 2MASS 0036+1821, 2MASS 1750−0016, and 2MASS 1043+2225 and many more limits on the Hα flux for late L dwarfs and T dwarfs (see Section 4). Our focus on these objects has allowed us to investigate the prevalence of magnetic activity in objects with low temperature atmospheres. The persistent magnetic emissions of many objects in this regime and the discovery of continued activity, even in late T dwarfs points to deficiencies in the understanding of magnetic atmospheric processes and/or new phenomena that fall outside of the standard paradigm of stellar activity.

For the warmer UCDs, chromospheric emission may still persist. Recent work by Rodríguez-Barrera et al. (2015) on the ability of UCD atmospheres to become magnetized suggests that the plasma conditions may allow for objects to remain magnetized down to an $T_{\rm eff} \sim 1400$ K, which is 900 K cooler than the similar magnetization threshold considered by Mohanty et al. (2002). This lower threshold is similar to the typical effective temperatures of L4/L5 dwarfs (Kirkpatrick 2005) and would coincide with where we see the detection of Hα emission bottom out (see Figure 10). However, for even cooler objects, the strong optical and radio emissions of some objects remain difficult to explain.

The emergence of the ECMI as a coherent explanation for the periodic radio emissions of numerous studies across the UCD regime provides an alternative. These studies argue that auroral processes are capable of driving the periodic radio and optical emissions that have been observed and are also consistent with potential long-term variability (see Section 5.1). The benchmark objects that have been used to investigate these processes have predominantly been systems of either late M or early L spectral types. These kinds of objects might exhibit both auroral and/or chromospheric emissions, requiring detailed study to distinguish. This confusion is alleviated when examining the population of late L dwarfs and T dwarfs with atmospheres for which standard Solar-like magnetic processes have difficulty generating chromospheric emissions, due to the highly neutral atmospheres. If the Hα emission in these objects is connected to the radio auroral emission, then the prevalence of this emission provides an estimate of the overall occurrence rate of auroral activity.

Our measurements of T dwarf Hα emission revealed that this activity indicator is less common than previously thought. B03

found three T dwarfs in about a dozen objects to exhibit this emission, two weak emitters and one very strong emitter. Our new observations and other work since their initial efforts show that the emission in this regime is actually much rarer and likely only seen in $\sim$7% of T dwarf systems. When considering objects of spectral type from L4 to T8, the detection rate remains only $9.2^{+3.5}_{-2.1}\%$ (as low as $8.5^{+3.3}_{-1.9}\%$ for L4–T9). It is possible that some of these targets exhibit variability and we did not observe the targets at the right point in time to catch the emission, however that is unlikely to be the case for all of the targets. Nevertheless, only extended monitoring of each target will be able to rule out that scenario.

Even if the occurrence rate of auroral activity is well characterized by our Hα detection rate of $\sim$10%, the question of the nature of the underlying mechanism that governs the emission still remains. Rodríguez-Barrera et al. (2015) point out that, despite having less magnetized atmospheres, objects with $T_{\rm eff} < 1400$ K are capable of sustaining significant ionospheres and driving auroral emission processes. Schrijver (2009) and Nichols et al. (2012) point to a rotation dominated magnetospheric–ionospheric coupling current system as the underlying mechanism for the auroral emissions capable of generating strong surface emission features near the magnetic poles. However, what determines whether an object displays auroral emission or not? One clue might be the long-term variability we have detected in the Hα emission of 2MASS 0036+1821. Within the auroral context, if this emission is proved to be related to the presence of satellites, then our observed detection rate for late L dwarfs and T dwarfs may reflect the satellite occurrence rate.

Comparing our overall Hα detection rate to surveys of brown dwarf radio emission revealed that radio and Hα detection rates in late L dwarfs and T dwarfs are comparable, suggesting that if the emission is auroral then geometric beaming may not play a prominent role in the detectability of the radio aurorae. Consequently, the sample of Hα emitting brown dwarfs are potentially excellent targets to pursue with sensitive radio telescopes, like the *Jansky Very Large Array*. These magnetically active brown dwarfs will be important benchmark objects for understanding not only magnetospheric processes across the brown dwarf regime from planets to stars but also for understanding magnetic dynamos in fully convective objects (Kao et al. 2016) and examining the upper atmospheric structures of brown dwarfs.

REFERENCES

Antonova, A., Hallinan, G., Doyle, J. G., et al. 2013, A&A, 549, A131
Apai, D., Radigan, J., Buenzli, E., et al. 2013, ApJ, 768, 121
Artigau, É., Bouchard, S., Doyon, R., & Lafrenière, D. 2009, ApJ, 701, 1534
Artigau, É., Doyon, R., Lafrenière, D., et al. 2006, ApJL, 651, L57
Badman, S. V., Branduardi-Raymont, G., Galand, M., et al. 2015, SSRv, 187, 99
Bardalez Gagliuffi, D. C., Burgasser, A. J., Gelino, C. R., et al. 2014, ApJ, 794, 143
Berger, E. 2002, ApJ, 572, 503
Berger, E. 2006, ApJ, 648, 629
Berger, E., Basri, G., Fleming, T. A., et al. 2010, ApJ, 709, 332
Berger, E., Rutledge, R. E., Phan-Bao, N., et al. 2009, ApJ, 695, 310
Berger, E., Rutledge, R. E., Reid, I. N., et al. 2005, ApJ, 627, 960
Bowler, B. P., Liu, M. C., & Dupuy, T. J. 2010, ApJ, 710, 45
Buenzli, E., Marley, M. S., Apai, D., et al. 2015, ApJ, 812, 163
Burgasser, A. J., Burrows, A., & Kirkpatrick, J. D. 2006a, ApJ, 639, 1095
Burgasser, A. J., Cruz, K. L., Cushing, M., et al. 2010, ApJ, 710, 1142
Burgasser, A. J., Geballe, T. R., Leggett, S. K., Kirkpatrick, J. D., & Golimowski, D. A. 2006b, ApJ, 637, 1067
Burgasser, A. J., Gillon, M., Faherty, J. K., et al. 2014, ApJ, 785, 48
Burgasser, A. J., Kirkpatrick, J. D., Brown, M. E., et al. 2002a, ApJ, 564, 421
Burgasser, A. J., Kirkpatrick, J. D., Liebert, J., & Burrows, A. 2003, ApJ, 594, 510
Burgasser, A. J., Kirkpatrick, J. D., Reid, I. N., et al. 2000a, AJ, 120, 473
Burgasser, A. J., Liebert, J., Kirkpatrick, J. D., & Gizis, J. E. 2002b, AJ, 123, 2744
Burgasser, A. J., Logsdon, S. E., Gagné, J., et al. 2015, ApJS, 220, 18
Burgasser, A. J., Reid, I. N., Leggett, S. K., et al. 2005, ApJL, 634, L177
Burgasser, A. J., Sitarski, B. N., Gelino, C. R., Logsdon, S. E., & Perrin, M. D. 2011, ApJ, 739, 49
Burgasser, A. J., Wilson, J. C., Kirkpatrick, J. D., et al. 2000b, AJ, 120, 1100
Burrows, A., Burgasser, A. J., Kirkpatrick, J. D., et al. 2002, ApJ, 573, 394
Burrows, A., Hubbard, W. B., Lunine, J. I., & Liebert, J. 2001, RvMP, 73, 719
Chiu, K., Fan, X., Leggett, S. K., et al. 2006, AJ, 131, 2722
Cooper, M. C., Newman, J. A., Davis, M., Finkbeiner, D. P., & Gerke, B. F. 2012, ascl:1203.003
Crossfield, I. J. M. 2014, A&A, 566, A130
Crossfield, I. J. M., Biller, B., Schlieder, J. E., et al. 2014, Natur, 505, 654
Cruz, K. L., Reid, I. N., Kirkpatrick, J. D., et al. 2007, AJ, 133, 439
Cruz, K. L., Reid, I. N., Liebert, J., Kirkpatrick, J. D., & Lowrance, P. J. 2003, AJ, 126, 2421
Cushing, M. C., Kirkpatrick, J. D., Gelino, C. R., et al. 2011, ApJ, 743, 50
Cushing, M. C., Marley, M. S., Saumon, D., et al. 2008, ApJ, 678, 1372
Cushing, M. C., Rayner, J. T., & Vacca, W. D. 2005, ApJ, 623, 1115
Deacon, N. R., Liu, M. C., Magnier, E. A., et al. 2011, AJ, 142, 77
Delorme, P., Willott, C. J., Forveille, T., et al. 2008, A&A, 484, 469
Dupuy, T. J., & Liu, M. C. 2012, ApJS, 201, 19
Dupuy, T. J., Liu, M. C., Leggett, S. K., et al. 2015, ApJ, 805, 56
Epchtein, N., de Batz, B., Capoani, L., et al. 1997, Msngr, 87, 27
Faber, S. M., Phillips, A. C., Kibrick, R. I., et al. 2003, Proc. SPIE, 4841, 1657
Faherty, J. K., Beletsky, Y., Burgasser, A. J., et al. 2014, ApJ, 790, 90
Faherty, J. K., Burgasser, A. J., Walter, F. M., et al. 2012, ApJ, 752, 56
Filippazzo, J. C., Rice, E. L., Faherty, J., et al. 2015, ApJ, 810, 158
Fleming, T. A., Liebert, J., Gioia, I. M., & Maccacaro, T. 1988, ApJ, 331, 958
Geballe, T. R., Knapp, G. R., Leggett, S. K., et al. 2002, ApJ, 564, 466
Hall, P. B. 2002, ApJL, 564, L89
Hallinan, G., Antonova, A., Doyle, J. G., et al. 2008, ApJ, 684, 644
Hallinan, G., Littlefair, S. P., Cotter, G., et al. 2015, Natur, 523, 568
Hamuy, M., Suntzeff, N. B., Heathcote, S. R., et al. 1994, PASP, 106, 566
Harding, L. K., Hallinan, G., Boyle, R. P., et al. 2013, ApJ, 779, 101
Heinze, A. N., Metchev, S., & Kellogg, K. 2015, ApJ, 801, 104
Jones, H. R. A., Pavlenko, Y., Viti, S., et al. 2005, MNRAS, 358, 105
Kaiser, N., Aussel, H., Burke, B. E., et al. 2002, Proc. SPIE, 4836, 154
Kao, M. M., Hallinan, G., Pineda, J. S., et al. 2016, ApJ, 818, 24
Kendall, T. R., Jones, H. R. A., Pinfield, D. J., et al. 2007, MNRAS, 374, 445
Kirkpatrick, J. D. 2005, ARA&A, 43, 195
Kirkpatrick, J. D., Barman, T. S., Burgasser, A. J., et al. 2006, ApJ, 639, 1120
Kirkpatrick, J. D., Cruz, K. L., Barman, T. S., et al. 2008, ApJ, 689, 1295
Kirkpatrick, J. D., Gelino, C. R., Cushing, M. C., et al. 2012, ApJ, 753, 156
Kirkpatrick, J. D., Reid, I. N., Liebert, J., et al. 1999, ApJ, 519, 802
Kirkpatrick, J. D., Reid, I. N., Liebert, J., et al. 2000, AJ, 120, 447
Kirkpatrick, J. D., Cushing, M. C., Gelino, C. R., et al. 2011, ApJS, 197, 19
Knapp, G. R., Leggett, S. K., Fan, X., et al. 2004, AJ, 127, 3553
Law, N. M., Kulkarni, S. R., Dekany, R. G., et al. 2009, PASP, 121, 1395
Lawrence, A., Warren, S. J., Almaini, O., et al. 2007, MNRAS, 379, 1599
Liebert, J., Kirkpatrick, J. D., Cruz, K. L., et al. 2003, AJ, 125, 343
Linsky, J. L., Bornmann, P. L., Carpenter, K. G., et al. 1982, ApJ, 260, 670
Liu, M. C., Dupuy, T. J., & Leggett, S. K. 2010, ApJ, 722, 311
Lodders, K. 1999, ApJ, 519, 793
Lynch, C., Murphy, T., Ravi, V., et al. 2016, MNRAS, 457, 1224
Lynch, C., Mutel, R. L., & Güdel, M. 2015, ApJ, 802, 106
Mace, G. N., Kirkpatrick, J. D., Cushing, M. C., et al. 2013, ApJS, 205, 6
Manjavacas, E., Goldman, B., Alcalá, J. M., et al. 2016, MNRAS, 455, 1341
Marley, M., & Robinson, T. 2015, ARA&A, 53, 279
Marley, M. S., Saumon, D., & Goldblatt, C. 2010, ApJL, 723, L117
Massey, P., & Gronwall, C. 1990, ApJ, 358, 344
McLean, I. S., McGovern, M. R., Burgasser, A. J., et al. 2003, ApJ, 596, 561
McLean, M., Berger, E., & Reiners, A. 2012, ApJ, 746, 23
Metchev, S. A., Heinze, A., Apai, D., et al. 2015, ApJ, 799, 154
Mohanty, S., Basri, G., Shu, F., Allard, F., & Chabrier, G. 2002, ApJ, 571, 469
Morton, T. D., & Winn, J. N. 2014, ApJ, 796, 47
Nakajima, T., Oppenheimer, B. R., Kulkarni, S. R., et al. 1995, Natur, 378, 463
Newman, J. A., Cooper, M. C., Davis, M., et al. 2013, ApJS, 208, 5
Nichols, J. D., Burleigh, M. R., Casewell, S. L., et al. 2012, ApJ, 760, 59
Oke, J. B., Cohen, J. G., Carr, M., et al. 1995, PASP, 107, 375
Oppenheimer, B. R., Kulkarni, S. R., Matthews, K., & Nakajima, T. 1995, Sci, 270, 1478
Patil, A., Huard, D., & Fonnesbeck, C. J. 2010, Journal of Statistical Software, 35, 1
Radigan, J., Jayawardhana, R., Lafrenière, D., et al. 2012, ApJ, 750, 105
Radigan, J., Lafrenière, D., Jayawardhana, R., & Artigau, E. 2014, ApJ, 793, 75
Reid, I. N., Burgasser, A. J., Cruz, K. L., Kirkpatrick, J. D., & Gizis, J. E. 2001, AJ, 121, 1710
Reid, I. N., Kirkpatrick, J. D., Gizis, J. E., et al. 2000, AJ, 119, 369
Reiners, A., & Basri, G. 2008, ApJ, 684, 1390
Rockosi, C., Stover, R., Kibrick, R., et al. 2010, Proc. SPIE, 7735, 0
Rodríguez-Barrera, M. I., Helling, C., Stark, C. R., & Rice, A. M. 2015, MNRAS, 454, 3977
Route, M., & Wolszczan, A. 2012, ApJL, 747, L22
Route, M., & Wolszczan, A. 2013, ApJ, 773, 18
Schmidt, S. J., Cruz, K. L., Bongiorno, B. J., Liebert, J., & Reid, I. N. 2007, AJ, 133, 2258
Schmidt, S. J., Hawley, S. L., West, A. A., et al. 2015, AJ, 149, 158
Schmidt, S. J., West, A. A., Bochanski, J. J., Hawley, S. L., & Kielty, C. 2014, PASP, 126, 642
Schrijver, C. J. 2009, ApJL, 699, L148
Schweitzer, A., Gizis, J. E., Hauschildt, P. H., Allard, F., & Reid, I. N. 2001, ApJ, 555, 368
Skrutskie, M. F., Cutri, R. M., Stiening, R., et al. 2006, AJ, 131, 1163
Stephens, D. C., Leggett, S. K., Cushing, M. C., et al. 2009, ApJ, 702, 154
Strauss, M. A., Fan, X., Gunn, J. E., et al. 1999, ApJL, 522, L61
Thorstensen, J. R., & Kirkpatrick, J. D. 2003, PASP, 115, 1207
Tinney, C. G., Burgasser, A. J., Kirkpatrick, J. D., & McElwain, M. W. 2005, AJ, 130, 2326
Treumann, R. A. 2006, A&ARv, 13, 229
Vasavada, A. R., Bouchez, A. H., Ingersoll, A. P., Little, B., & Anger, C. D. 1999, JGR, 104, 27133
Walkowicz, L. M., Johns-Krull, C. M., & Hawley, S. L. 2008, ApJ, 677, 593

Williams, P. K. G., & Berger, E. 2015, ApJ, 808, 189

Williams, P. K. G., Cook, B. A., & Berger, E. 2014, ApJ, 785, 9

Winn, J. N. 2010, Exoplanets, ed. S. Seager (Tucson, AZ: University of Arizona Press), 526

Wright, E. L., Eisenhardt, P. R. M., Mainzer, A. K., et al. 2010, AJ, 140, 1868

York, D. G., Adelman, J., Anderson, J. E., Jr., et al. 2000, AJ, 120, 1579

Zapatero Osorio, M. R., Martín, E. L., Bouy, H., et al. 2006 ApJ, 647, 1405